

## DATA PAPER

G. A. D. SAVORGNAN<sup>1</sup> AND A. W. GRAHAM<sup>1</sup>

Centre for Astrophysics and Supercomputing, Swinburne University of Technology, Hawthorn, Victoria 3122, Australia.

*Draft version February 13, 2015*

## ABSTRACT

abstract

*Subject headings:* keywords

### 1. INTRODUCTION

Supermassive black holes and host bulges have very different sizes. If the event horizon of the Galactic supermassive black hole was as big as a grain of sand of the Sahara desert, then the black hole gravitational sphere-of-influence would be as big as the international airport of Cairo, and the Galactic bulge would be as big as the Sahara desert itself. It is thus surprising that the masses of supermassive black holes ( $M_{\text{BH}}$ ) scale with a number of properties of their host bulges, indicating the non-gravitational origin of these correlations (e.g. Dressler 1989; Yee 1992; Kormendy & Richstone 1995; Laor et al. 1997; Magorrian et al. 1998; Ferrarese & Merritt 2000; Gebhardt et al. 2000; Graham et al. 2001; Marconi & Hunt 2003; Häring & Rix 2004; Graham 2012; Graham & Scott 2015).

The tightness of (i.e. the small scatter about) the observed black hole mass correlations has led to the idea that black holes and host galaxies have coevolved with some sort of self-regulated growth. Exploring the evolution of this growth with cosmic time could help identify the driving mechanisms of the black hole – galaxy coevolution. Observations at  $z = 0$  set the local benchmark from which to measure this evolution. Any complete theory or model describing the coevolution of galaxies and black holes must incorporate all of the observed scaling relations, which also have to be consistent with each other. Modern hydrodynamical simulations, such as EAGLE (Schaye et al. 2015), calibrate the feedback efficiencies to match the  $z = 0$  black hole mass – galaxy mass relation. Such scaling relations can also be employed to predict the masses of black holes in other galaxies, where a direct measure of  $M_{\text{BH}}$  would be extremely time consuming or simply impossible due to technological limitations. Moreover, many accurate  $M_{\text{BH}}$  predictions enable one to derive the local black hole mass function (e.g. Salucci et al. 1999; Graham et al. 2007) and space density (e.g. Graham & Driver 2007b; Comastri et al. 2015). All of these examples depend on the  $z = 0$  relations, and as such the recalibration of the black hole mass – bulge stellar mass ratio ( $M_{\text{BH}}/M_{*,\text{sph}}$ ) in large bulges, from 0.1 – 0.2% (e.g. Häring & Rix 2004) to 0.36% (Graham 2012) and then 0.49% (Graham & Scott 2015), has many substantial implications.

Since the early stellar dynamical detections of black holes were carried out in the '80s (see the references in the reviews by Kormendy & Richstone 1995, Richstone et al. 1998 and Graham 2015 for pioneering papers), the num-

ber of (direct) black hole mass measurements has increased with time and it has recently become a statistically meaningful sample with which one can study SMBH demographics. It is now generally accepted that supermassive black holes reside at the center of most, if not all, massive galaxies, either quiescent or active.

Massive, early-type galaxies are often composite systems. The knowledge that many “elliptical” galaxies actually contain embedded stellar disks dates back at least three decades (Capaccioli 1987; Carter 1987; Rix & White 1990; Bender 1990; Scorza & Bender 1990; Nieto et al. 1991; Rix & White 1992; Scorza & Bender 1995). After examining long-slit and integral field unit spectroscopic observations of morphologically classified elliptical galaxies in the Fornax cluster, D’Onofrio et al. (1995), Graham et al. (1998) and Scott et al. (2014) concluded that only 3 bright galaxies do not harbour a disk-like component. Larger surveys with integral field spectrographs of early-type galaxies, such as the ATLAS<sup>3D</sup> Project (Cappellari et al. 2011), have further advanced this view of “elliptical” galaxies being all but simple and featureless pressure-supported systems. More than half of all morphologically classified elliptical galaxies in the ATLAS<sup>3D</sup> sample are fast rotators (Emsellem et al. 2011). Krajnović et al. (2013) showed that “fast rotators” as a class are disk-galaxies or at least disk-like galaxies. In their magnitude-limited survey, systems without any signature of disk-like components (neither in the kinematics nor in the photometry) dominate only the most massive end (beyond  $10^{11.5} M_{\odot}$ ) of the distribution. Given the prevalence of disks, it is clearly important to perform bulge/disk decompositions, if one is to properly explore the black hole-bulge connection. Indeed, separating the disk light from that of the bulge has led to the discovery of the missing population of compact, massive spheroids in the local Universe (Graham, Dullo, Savorgnan 2015). If we are to properly understand the evolution of galaxies, we need to understand their components.

Measuring the photometric and structural properties of a galaxy’s spheroidal component requires the ability to separate it from the rest of the galaxy. Such galaxy decomposition involves a parametric analysis that allows one to fit the surface brightness distribution of galaxies using a combination of analytic functions (usually one function per galaxy component, such as bulges, disks, bars, nuclei, etc.). The one-dimensional (1D) technique involves fitting isophotes to the galaxy image, extracting the (one-dimensional) surface brightness radial profile and modeling it with a combination of analytic func-

tions. With the two-dimensional (2D) technique, one fits analytic functions directly to the 2D images.

Over the past eight years, five independent studies (Graham & Driver 2007a; Sani et al. 2011; Vika et al. 2012; Beifiori et al. 2012; Läscher et al. 2014a,b) have attempted galaxy decomposition in order to derive the bulge parameters and explore their relation with the black hole masses. **Rusli has explored the black hole - core relation.** Interestingly, the past studies used almost the same sample of galaxies, yet they claimed some contradictory conclusions. For example, one study (Graham & Driver 2007a) obtained a good  $M_{\text{BH}} - n_{\text{sph}}$  correlation (the bulge Sérsic index  $n_{\text{sph}}$  is a measure of the central radial concentration of stars, Trujillo et al. 2001), whereas the remaining four did not. In addition, Läscher et al. (2014b) **who did not work at 3.6 $\mu\text{m}$**  declared that  $M_{\text{BH}}$  correlates equally well with the total galaxy luminosity and the bulge luminosity, as opposed to Beifiori et al. (2012), who claimed that the bulge mass is a better tracer of  $M_{\text{BH}}$  than the galaxy mass. The past studies did not converge to the same conclusions because their best-fit models for the same galaxy were often significantly different and not consistent with each other in terms of fitted components. Moreover, none of these studies attempted an individual galaxy-by-galaxy comparison of their models with the previous literature. We have now made this comparison and performed the optimal decompositions, using 3.6  $\mu\text{m}$  *Spitzer* satellite imagery, which is an excellent proxy for the stellar mass, superior to the *K*-band (Sheth et al. 2010 and references therein). We will use these in a series of forthcoming papers to obtain improved black hole mass scaling relations using the largest sample (66) of galaxies to date.

This paper is structured as follows. Section 2 presents the galaxy sample and imaging data-set used to conduct this study. Section 3 describes how we performed the galaxy decompositions, i.e. how we identified and modeled the sub-components that constitute our galaxies. In Section 4 we outline the results from our analysis and discuss the error analysis. Section 5 summarizes our main conclusions. The individual galaxy decompositions are made available in the electronic version of this manuscript.

## 2. DATA

Our initial galaxy sample (see Table 1) consists of 75 objects for which a dynamical detection of the black hole mass had been reported in the literature at the time we started this project, and for which at least one 3.6  $\mu\text{m}$  *Spitzer*/IRAC<sup>1</sup> observation was publicly available. Black hole masses were drawn from the catalog of Graham & Scott (2013) for 70 galaxies, from Rusli et al. (2013b) for 4 galaxies and from Greenhill et al. (2003) for 1 galaxy. As explained in Section 4, this initial sample was ultimately reduced to 66 galaxies for which useful bulge parameters could be obtained.

### 2.1. *Spitzer*/IRAC observations

#### 2.1.1. Data acquisition

For each of our 75 galaxies, we downloaded from the *Spitzer* Heritage Archive<sup>2</sup> all the available 3.6  $\mu\text{m}$  IRAC Astronomical Observation Requests (AORs), listed in Table 2. Each AOR is an individual *Spitzer* observation sequence, and includes a number of data frames (the individual exposures) and the calibration data. The data frames were selected to be corrected Basic Calibrated Data (cBCD), produced by the IRAC Level 1 pipeline. This automatic pipeline takes a single “raw” image, removes the scattered light, and performs dark subtraction, flatfielding correction and flux calibration (into units of MJy sr<sup>-1</sup>). The final product (the BCD) is a flux-calibrated image which has had all the well-understood instrumental signatures removed. BCD frames are further processed through an “artifact correction” pipeline that mitigates the commonly found artifacts of stray light, saturation, “muxbleed” and column pulldown<sup>3</sup>. After the artifact correction has been applied, the BCD becomes a cBCD.

#### 2.1.2. Mosaicking

We performed image mosaicking using the MOPEX package (Makovoz & Marleau 2005). This enabled the production of suitably wide-field-of-view images for accurate sky background subtraction. Individual cBCD frames with exposure time of 1 sec were rejected. Permanent or semi-permanent bad pixels, contained in a semi-static mask (the “pmask”), were ignored. Each AOR is associated to a specific pmask. Therefore, when multiple AORs were available for the same galaxy, we merged the different pmasks. Cosmic ray rejection was performed with the dual outlier and multi-frame techniques. The pixel size of the mosaic was set to be the same as the input cBCD frames (1''.22  $\times$  1''.22). For 3.6  $\mu\text{m}$  observations with this pixel scale, the photometric zeropoint magnitude is  $m_{\text{zp}} = 17.26$  mag. The orientation of the mosaic was set to the average rotation angle of the input cBCD frames. Individual cBCD frames were combined together into a single mosaic with the default linear interpolation algorithm.

#### 2.1.3. Overlap correction

Before generating a mosaic, MOPEX can perform background matching among the individual frames by using the *overlap* module. This module calculates and applies an additive correction to the individual frames, producing a consistent background across the mosaicked image. According to the *Spitzer Data Cookbook*, the use of the *overlap* module is not particularly recommended for 3.6  $\mu\text{m}$  observations. However, after a visual inspection of the mosaics obtained without activating the *overlap* module, we found that all the mosaics obtained from multiple AORs were affected by patchiness, due to bias fluctuations in the CCD array. For this reason, we re-generated the multiple-AORs mosaics by activating

<sup>2</sup> <http://irsa.ipac.caltech.edu/applications/Spitzer/SHA/>

<sup>3</sup> Stray light includes scattered light from stars outside the array location as well as filter ghosts from bright stars. Multiplexer bleed, or “muxbleed”, can be generated by stars, hot pixels, and particle hits. It appears as a decaying trail of pixels, repeating every fourth column. “Column pulldown” is caused by a bright pixel that triggers a bias shift within its respective column, creating a lower background value throughout the entire column than in the surrounding columns.

<sup>1</sup> IRAC is the InfraRed Array Camera onboard the *Spitzer* Space Telescope.

TABLE 1

**Galaxy sample.** *Column (1):* GALAXY NAME. *Column (2):* DISTANCE. *Column (3):* BLACK HOLE MASS. *Column (4):* REFERENCE OF THE BLACK HOLE MASS REPORTED HERE (G+03 = GREENHILL ET AL. 2003, GS13 = GRAHAM & SCOTT 2013; R+13b = RUSLI ET AL. 2013b). *Column (5):* PRESENCE OF A PARTIALLY DEPLETED CORE. THE QUESTION MARK IS USED WHEN THE CLASSIFICATION HAS COME FROM THE VELOCITY DISPERSION CRITERIA MENTIONED IN SECTION 2.2.3. THE VALUE OF THE CORE BREAK RADIUS IS REPORTED IN PARENTHESIS WHEN AVAILABLE. *Column (6):* REFERENCE OF THE IDENTIFICATION OF A PARTIALLY DEPLETED CORE (G+94 = GRILLMAIR ET AL. 1994; F+97 = FORBES ET AL. 1997; Q+00 = QUILLEN ET AL. 2000, T+04 = TRUJILLO ET AL. 2004; F+06 = FERRARESE ET AL. 2006; J+11 = JARDEL ET AL. 2011; R+11 = RICHINGS ET AL. 2011; DG13 = DULLO & GRAHAM 2013; R+13a = RUSLI ET AL. 2013a). *Column (7):* KINEMATICAL CLASSIFICATION (FAST/SLOW ROTATOR). *Column (8):* AVAILABILITY OF VELOCITY MAP (A = ATLAS<sup>3D</sup>, S = SLUGGS). *Column (9):* COMPLETION OF 1D FIT. *Column (10):* COMPLETION OF 2D FIT.

Galaxy	Distance	$M_{\text{BH}}$	Ref.	Core	Ref.	Rot.	Vel. map	1D fit	2D fit
(1)	(2)	(3)	(4)	(5)	(6)	(7)	(8)	(9)	(10)
Circinus	4.0	$0.017^{+0.004}_{-0.003}$	G+03	no?				no	no
IC 1459	28.4	$24^{+10}_{-10}$	GS13	yes (0.7)	R+13a			yes	yes
IC 2560	40.7	$0.044^{+0.044}_{-0.022}$	GS13	no?				yes	no
IC 4296	40.7	$11^{+2}_{-2}$	GS13	yes?				yes	yes
M104	9.5	$6.4^{+0.4}_{-0.4}$	GS13	yes	J+11			yes	no
M105	10.3	$4^{+1}_{-1}$	GS13	yes (1.1)	DG13, R+13a	FAST	A	yes	yes
M106	7.2	$0.39^{+0.01}_{-0.01}$	GS13	no				yes	no
M31	0.7	$1.4^{+0.9}_{-0.3}$	GS13	no				yes	no
M32	0.8	$0.024^{+0.005}_{-0.005}$	GS13	no				no	no
M49	17.1	$25^{+3}_{-1}$	R+13b	yes (1.5)	DG13, R+13a	SLOW	A	yes	yes
M59	17.8	$3.9^{+0.4}_{-0.4}$	GS13	no		FAST	A	yes	no
M60	16.4	$47^{+10}_{-10}$	GS13	yes (2.7)	DG13, R+13a	FAST	A, S	no	no
M64	7.3	$0.016^{+0.004}_{-0.004}$	GS13	no?				yes	no
M77	15.2	$0.084^{+0.003}_{-0.003}$	GS13	no				no	no
M81	3.8	$0.74^{+0.21}_{-0.11}$	GS13	no				yes	no
M84	17.9	$9.0^{+0.9}_{-0.8}$	GS13	yes (1.9)	F+06	SLOW	A, S	yes	yes
M87	15.6	$58.0^{+3.5}_{-3.5}$	GS13	yes (7.2)	F+06	SLOW	A, S	yes	yes
M89	14.9	$4.7^{+0.5}_{-0.5}$	GS13	yes (0.4)	DG13, R+13a	SLOW	A	yes	no
M94	4.4	$0.060^{+0.014}_{-0.014}$	GS13	no?				yes	no
M96	10.1	$0.073^{+0.015}_{-0.015}$	GS13	no				yes	yes
NGC 0253	3.5	$0.10^{+0.10}_{-0.05}$	GS13	no				no	no
NGC 0524	23.3	$8.3^{+2.7}_{-1.3}$	GS13	yes (0.2)	R+11	FAST	A	yes	no
NGC 0821	23.4	$0.39^{+0.26}_{-0.09}$	GS13	no		FAST	A, S	yes	yes
NGC 1023	11.1	$0.42^{+0.04}_{-0.04}$	GS13	no		FAST	A, S	yes	yes
NGC 1300	20.7	$0.73^{+0.69}_{-0.35}$	GS13	no				yes	no
NGC 1316	18.6	$1.50^{+0.75}_{-0.80}$	GS13	no		FAST		yes	no
NGC 1332	22.3	$14^{+2}_{-2}$	GS13	no				yes	no
NGC 1374	19.2	$5.8^{+0.5}_{-0.5}$	R+13b	no?		FAST	A	yes	yes
NGC 1399	19.4	$4.7^{+0.6}_{-0.6}$	GS13	yes (2.4)	DG13, R+13a	SLOW	A	yes	no
NGC 2273	28.5	$0.083^{+0.004}_{-0.004}$	GS13	no				yes	no
NGC 2549	12.3	$0.14^{+0.02}_{-0.13}$	GS13	no		FAST	A	yes	yes
NGC 2778	22.3	$0.15^{+0.09}_{-0.10}$	GS13	no		FAST	A	yes	no
NGC 2787	7.3	$0.40^{+0.04}_{-0.05}$	GS13	no				yes	no
NGC 2974	20.9	$1.7^{+0.2}_{-0.2}$	GS13	no		FAST	A, S	yes	yes
NGC 3079	20.7	$0.024^{+0.024}_{-0.012}$	GS13	no?				yes	no
NGC 3091	51.2	$36^{+1}_{-2}$	R+13b	yes (0.6)	R+13a			yes	yes
NGC 3115	9.4	$8.8^{+10.0}_{-2.7}$	GS13	no				yes	no
NGC 3227	20.3	$0.14^{+0.10}_{-0.06}$	GS13	no				yes	no
NGC 3245	20.3	$2.0^{+0.5}_{-0.5}$	GS13	no		FAST	A	yes	yes
NGC 3377	10.9	$0.77^{+0.04}_{-0.06}$	GS13	no		FAST	A, S	yes	yes
NGC 3384	11.3	$0.17^{+0.01}_{-0.02}$	GS13	no		FAST	A	yes	no
NGC 3393	55.2	$0.34^{+0.02}_{-0.02}$	GS13	no				yes	yes
NGC 3414	24.5	$2.4^{+0.3}_{-0.3}$	GS13	no		SLOW	A	yes	no
NGC 3489	11.7	$0.058^{+0.008}_{-0.008}$	GS13	no		FAST	A	yes	yes
NGC 3585	19.5	$3.1^{+1.4}_{-0.6}$	GS13	no				yes	no
NGC 3607	22.2	$1.3^{+0.5}_{-0.5}$	GS13	no		FAST	A	yes	yes
NGC 3608	22.3	$2.0^{+1.1}_{-0.6}$	GS13	yes (0.2)	DG13, R+13a	SLOW	A, S	yes	yes
NGC 3842	98.4	$97^{+30}_{-26}$	GS13	yes (0.7)	DG13, R+13a			yes	no
NGC 3998	13.7	$8.1^{+2.0}_{-1.9}$	GS13	no		FAST	A	yes	no
NGC 4026	13.2	$1.8^{+0.6}_{-0.3}$	GS13	no		FAST	A	yes	no
NGC 4151	20.0	$0.65^{+0.07}_{-0.07}$	GS13	no				yes	no

Galaxy	Distance	$M_{\text{BH}}$	Ref.	Core	Ref.	Rot.	Vel. map	1D fit	2D fit
(1)	[Mpc] (2)	$[10^8 M_{\odot}]$ (3)	(4)	([arcsec]) (5)	(6)	(7)	(8)	(9)	(10)
NGC 4261	30.8	$5^{+1}_{-1}$	GS13	yes (1.6)	R+11	SLOW	A	yes	yes
NGC 4291	25.5	$3.3^{+0.9}_{-2.5}$	GS13	yes (0.3)	DG13, R+13a			yes	yes
NGC 4342	23.0	$4.5^{+2.3}_{-1.5}$	GS13	no		FAST	A	no	no
NGC 4388	17.0	$0.075^{+0.002}_{-0.002}$	GS13	no?				yes	no
NGC 4459	15.7	$0.68^{+0.13}_{-0.13}$	GS13	no		FAST	A	yes	no
NGC 4473	15.3	$1.2^{+0.4}_{-0.9}$	GS13	no		FAST	A, S	yes	yes
NGC 4486A	17.0	$0.13^{+0.08}_{-0.08}$	GS13	no		FAST	A	no	no
NGC 4564	14.6	$0.60^{+0.03}_{-0.09}$	GS13	no		FAST	A	yes	no
NGC 4596	17.0	$0.79^{+0.38}_{-0.33}$	GS13	no		FAST	A	yes	no
NGC 4697	11.4	$1.8^{+0.2}_{-0.1}$	GS13	no		FAST	A, S	yes	yes
NGC 4889	103.2	$210^{+160}_{-160}$	GS13	yes (1.7)	F+97			yes	yes
NGC 4945	3.8	$0.014^{+0.014}_{-0.007}$	GS13	no?				yes	yes
NGC 5077	41.2	$7.4^{+4.7}_{-3.0}$	GS13	yes (0.3)	T+04			yes	yes
NGC 5128	3.8	$0.45^{+0.17}_{-0.10}$	GS13	no?				yes	no
NGC 5576	24.8	$1.6^{+0.3}_{-0.4}$	GS13	no		SLOW	A	yes	yes
NGC 5813	31.3	$6.8^{+0.7}_{-0.7}$	GS13	yes (0.4)	DG13, R+13a	SLOW	A	no	no
NGC 5845	25.2	$2.6^{+0.4}_{-1.5}$	GS13	no		FAST	A	yes	yes
NGC 5846	24.2	$11^{+1}_{-1}$	GS13	yes	F+97	SLOW	A, S	yes	yes
NGC 6251	104.6	$5^{+2}_{-2}$	GS13	yes?				yes	yes
NGC 7052	66.4	$3.7^{+2.6}_{-1.5}$	GS13	yes (0.8)	Q+00			yes	yes
NGC 7582	22.0	$0.55^{+0.26}_{-0.19}$	GS13	no				no	no
NGC 7619	51.5	$25^{+8}_{-3}$	R+13b	yes (0.5)	DG13, R+13a			yes	no
NGC 7768	112.8	$13^{+5}_{-4}$	GS13	yes	G+94			yes	no
UGC 03789	48.4	$0.108^{+0.005}_{-0.005}$	GS13	no?				yes	no

TABLE 2

**Astronomical observation request log.** *Column (1):* GALAXY NAME. *Column (2):* PROGRAM IDENTIFICATION NUMBER. *Column (3):* RIGHT ASCENSION. *Column (4):* DECLINATION. *Column (5):* OBSERVATION START TIME. *Column (6):* OBSERVATION IDENTIFICATION NUMBER.

Galaxy (1)	Program ID (2)	RA (J2000) (3)	Dec (J2000) (4)	Start time (5)	AORKEY (6)
Circinus	40936	14h13m09.91s	-65d20m20.5s	2007-09-09	22108160
	50173	14h13m09.91s	-65d20m20.5s	2009-03-20	25705472
	50173	14h13m13.91s	-65d21m30.0s	2009-03-20	25705728
IC1459	20371	22h57m10.61s	-36d27m44.0s	2005-11-27	14570240
IC2560	40936	10h16m19.30s	-33d33m53.0s	2007-07-04	22104576
	61009	10h16m19.27s	-33d33m53.2s	2010-01-23	35377664
IC4296	20371	13h36m39.05s	-33d57m57.2s	2006-02-12	14571008
M31	30192	0h40m54.40s	+40d53m50.3s	2008-02-02	17863424
	30192	0h42m42.38s	+41d08m45.5s	2007-02-19	17862656
	30192	0h42m55.95s	+41d03m22.0s	2008-02-02	17862912
	3126	0h39m14.63s	+40d16m08.5s	2005-01-20	12551168
	3126	0h39m14.63s	+40d16m08.5s	2005-01-20	12551424
	3126	0h39m14.63s	+40d16m08.5s	2005-01-20	12551936
	3126	0h39m14.63s	+40d16m08.5s	2005-01-20	12552448
	3126	0h39m16.31s	+40d15m10.0s	2005-08-18	15215360
	3126	0h39m16.31s	+40d15m10.0s	2005-08-19	15214848
	3126	0h39m17.31s	+40d15m00.0s	2005-08-19	15213312
	3126	0h39m17.31s	+40d15m00.0s	2005-08-19	15213568
	3126	0h42m44.32s	+41d16m08.5s	2005-01-20	12551680
	3126	0h42m44.32s	+41d16m08.5s	2005-01-20	12552192
	3126	0h42m44.32s	+41d16m08.5s	2005-01-20	12552704
	3126	0h42m44.32s	+41d16m08.5s	2005-01-20	12552960
	3126	0h42m44.32s	+41d16m08.5s	2005-01-20	12553216
	3126	0h42m44.32s	+42d16m08.5s	2005-01-19	12553472
	3126	0h42m44.32s	+42d16m08.5s	2005-01-19	12553728
	3126	0h42m46.00s	+41d15m00.0s	2005-08-18	15213824
	3126	0h42m46.00s	+41d15m00.0s	2005-08-18	15214080
	3126	0h42m46.00s	+41d15m00.0s	2005-08-18	15214336
	3126	0h45m23.97s	+41d16m08.5s	2005-01-20	12550912
	3126	0h45m23.97s	+41d16m08.5s	2005-01-21	12550656
	3126	0h45m25.61s	+41d15m00.0s	2005-08-18	15214592
	3126	0h45m25.61s	+41d15m00.0s	2005-08-18	15215104
	3362	0h43m02.42s	+41d12m56.7s	2005-01-16	12237312
	3400	0h40m32.46s	+41d21m27.2s	2005-07-22	10883072
	3400	0h42m34.42s	+41d14m01.6s	2005-01-19	10883840
	3400	0h42m42.00s	+40d51m54.0s	2005-01-18	10885376
	3400	0h42m42.00s	+40d51m54.0s	2005-01-18	10885376
	3400	0h42m44.00s	+41d16m06.0s	2005-01-19	10885120
	3400	0h42m59.60s	+41d19m19.3s	2005-07-23	10884096
	3400	0h44m29.78s	+41d21m36.6s	2005-01-21	10884608
	61001	0h44m23.90s	+41d22m48.0s	2010-02-05	33176576
	61001	0h44m23.90s	+41d22m48.0s	2010-02-13	33175808
	61001	0h44m23.90s	+41d22m48.0s	2010-02-25	33175040
	61001	0h44m23.90s	+41d22m48.0s	2010-03-08	33174528
	61001	0h44m23.90s	+41d22m48.0s	2010-09-02	33174016
	61001	0h44m23.90s	+41d22m48.0s	2010-09-11	33208832
	61001	0h44m23.90s	+41d22m48.0s	2010-09-23	33208320
	61001	0h44m23.90s	+41d22m48.0s	2010-10-04	33207808
	61001	0h44m23.90s	+41d22m48.0s	2011-02-09	33207040
	61001	0h44m23.90s	+41d22m48.0s	2011-02-20	33182720
	61001	0h44m23.90s	+41d22m48.0s	2011-03-02	33182208
	61001	0h44m23.90s	+41d22m48.0s	2011-03-12	33181696
	69	0h42m41.80s	+40d51m52.0s	2004-07-19	4425728
	70062	0h45m34.20s	+41d09m19.0s	2011-02-09	41067520
	70062	0h45m43.39s	+41d13m18.3s	2011-02-09	41067008
M49	20606	12h29m21.31s	+8d09m23.7s	2006-02-09	16851456
	20606	12h29m30.26s	+7d59m34.4s	2006-02-09	16853504
	20606	12h30m05.09s	+8d04m23.6s	2006-02-09	16856832
	61068	12h29m46.80s	+8d00m01.4s	2011-03-15	41211904
	61068	12h29m46.80s	+8d00m01.4s	2011-07-22	41211392
	69	12h29m38.60s	+7d49m25.0s	2005-01-22	4468992
	69	12h29m46.40s	+7d59m47.0s	2004-07-01	4469760
	80134	12h29m44.31s	+7d48m23.5s	2011-07-22	42565888
M59	3649	12h42m02.32s	+11d38m48.9s	2005-06-10	11377408
M60	69	12h43m39.60s	+11d33m08.0s	2004-06-10	4476672
M64	159	12h56m43.76s	+21d40m51.9s	2004-05-27	5513472
	159	12h56m43.76s	+21d40m51.9s	2004-06-09	5513216
M77	32	2h42m40.86s	-0d00m46.2s	2004-01-16	3898624
	80089	2h42m40.71s	-0d00m47.8s	2011-09-21	42524928
M81	1035	9h55m33.17s	+69d03m55.1s	2003-11-06	6629120
	1101	9h55m33.17s	+69d03m55.1s	2003-12-04	7893760

Galaxy (1)	Program ID (2)	RA (J2000) (3)	Dec (J2000) (4)	Start time (5)	AORKEY (6)
	1101	9h55m33.17s	+69d03m55.1s	2003-12-04	7894016
	1101	9h55m33.17s	+69d03m55.1s	2003-12-04	7894272
	1101	9h55m33.17s	+69d03m55.1s	2003-12-04	7894528
	1101	9h55m33.17s	+69d03m55.1s	2003-12-04	7894784
	1101	9h55m33.17s	+69d03m55.1s	2003-12-04	7895040
	1101	9h55m33.17s	+69d03m55.1s	2003-12-04	7895296
	1101	9h55m33.17s	+69d03m55.1s	2003-12-04	7895552
	121	9h55m33.17s	+69d03m55.1s	2004-12-21	12485888
	121	9h55m33.17s	+69d03m55.1s	2005-05-06	12485632
	121	9h55m33.17s	+69d03m55.1s	2005-10-24	12486144
	159	9h55m33.17s	+69d03m55.1s	2004-05-01	5503488
	159	9h55m33.17s	+69d03m55.1s	2004-05-01	5503744
	40118	9h55m33.17s	+69d03m55.1s	2008-04-11	22353664
	40118	9h55m33.17s	+69d03m55.1s	2008-04-11	22357504
	40118	9h55m33.17s	+69d03m55.1s	2008-04-11	22357760
	40118	9h55m33.17s	+69d03m55.1s	2008-04-11	22358016
	40118	9h55m33.17s	+69d03m55.1s	2008-04-12	22358272
	40118	9h55m33.17s	+69d03m55.1s	2008-04-12	22358528
	40118	9h55m33.17s	+69d03m55.1s	2008-05-12	23752192
	40118	9h55m33.17s	+69d03m55.1s	2008-05-13	23751936
	40204	9h53m48.50s	+68d58m08.0s	2007-11-13	22604800
	40204	9h53m48.50s	+68d58m08.0s	2007-11-22	22604544
	40204	9h57m32.00s	+69d02m45.0s	2007-11-15	22537472
	40204	9h57m32.00s	+69d02m45.0s	2007-11-15	22537728
	40204	9h57m32.60s	+69d17m00.0s	2007-11-15	22603520
	40204	9h57m32.60s	+69d17m00.0s	2007-11-15	22603776
	40619	9h55m24.77s	+69d01m13.7s	2007-11-15	23106816
	40714	9h57m54.05s	+69d03m47.3s	2007-11-13	23173888
M84	69	12h25m03.60s	+12d53m14.0s	2004-05-27	4463872
M87	3228	12h30m49.42s	+12d23m28.0s	2005-06-11	10483200
	3228	12h30m49.42s	+12d23m28.0s	2005-06-11	10483200
	3228	12h30m49.42s	+12d23m28.0s	2005-06-11	12673792
	50795	12h30m49.42s	+12d23m28.0s	2008-07-15	26921984
M89	159	12h35m39.82s	+12d33m22.6s	2004-05-27	5540608
	159	12h35m39.82s	+12d33m22.6s	2004-06-10	5540352
M94	159	12h50m53.06s	+41d07m13.6s	2004-05-21	5509376
	159	12h50m53.06s	+41d07m13.6s	2004-05-24	5509120
M96	69	10h46m46.90s	+11d49m29.0s	2004-05-19	4444160
M104	159	12h39m59.43s	-11d37m23.0s	2004-06-10	5518080
	159	12h39m59.43s	-11d37m23.0s	2005-01-22	5517824
M105	69	10h47m49.50s	+12d34m56.0s	2004-12-15	4445696
M106	20801	12h18m57.52s	+47d18m14.2s	2005-12-24	15189248
	61002	12h19m17.00s	+47d12m10.0s	2010-01-12	31538688
	61002	12h19m17.00s	+47d12m10.0s	2010-01-29	31538176
	61002	12h19m17.00s	+47d12m10.0s	2010-02-07	31537664
	61002	12h19m17.00s	+47d12m10.0s	2010-02-26	31537152
	61002	12h19m17.00s	+47d12m10.0s	2010-06-06	31536896
	61002	12h19m17.00s	+47d12m10.0s	2010-06-21	31536640
	61002	12h19m17.00s	+47d12m10.0s	2010-07-03	31536384
	61002	12h19m17.00s	+47d12m10.0s	2010-07-17	31523584
	61002	12h19m17.00s	+47d12m10.0s	2011-01-17	31523072
	61002	12h19m17.00s	+47d12m10.0s	2011-02-09	31522560
	61002	12h19m17.00s	+47d12m10.0s	2011-06-15	31539712
	61002	12h19m17.00s	+47d12m10.0s	2011-06-27	31539200
	61008	12h18m57.50s	+47d18m14.3s	2010-01-14	35331072
NGC 0253	30542	0h46m46.56s	-25d21m50.4s	2006-08-11	18378496
	30542	0h46m47.04s	-25d06m50.4s	2006-08-11	18377984
	30542	0h47m26.40s	-25d15m03.6s	2006-08-12	18377728
	30542	0h48m02.64s	-25d05m24.0s	2006-08-12	18378240
	30542	0h48m03.12s	-25d24m10.8s	2006-08-12	18378752
NGC 0524	50630	1h24m47.72s	+9d32m19.8s	2008-09-18	26603264
	60166	1h24m57.23s	+9d33m01.5s	2009-08-22	35009024
	60166	1h24m57.23s	+9d33m01.5s	2010-02-16	35009280
NGC 0821	20371	2h08m21.14s	+10d59m41.7s	2005-08-21	14569216
NGC 1023	69	2h40m24.00s	+39d03m47.8s	2004-02-11	4432640
NGC 1194	3269	3h03m49.11s	-1d06m13.4s	2005-01-16	12464640
NGC 1277	3228	3h19m48.16s	+41d30m42.1s	2005-02-20	10483456
	80089	3h19m48.16s	+41d30m42.1s	2011-10-24	42372864
NGC 1300	61009	3h19m40.94s	-19d24m39.9s	2009-10-04	35388416
	61065	3h19m41.90s	-19d24m52.2s	2009-09-05	37317376
NGC 3393	61009	10h48m23.46s	-25d09m43.4s	2010-02-06	38703104
NGC 3414	50630	10h51m16.23s	+27d58m30.0s	2009-01-29	26603520
	61063	10h51m15.80s	+27d50m55.4s	2011-02-11	31016448
NGC 3489	69	11h00m18.10s	+13d54m08.0s	2004-05-19	4448000
NGC 3585	30318	11h13m17.11s	-26d45m18.0s	2006-07-08	18033152
NGC 3607	69	11h16m54.00s	+18d03m11.0s	2004-05-18	4449536
NGC 3608	30318	11h16m58.96s	+18d08m54.9s	2006-12-27	18033408
NGC 3842	25	11h44m30.00s	+19d50m00.0s	2005-06-13	3858688
	40301	11h43m49.11s	+19d58m06.2s	2009-02-02	21990656
	61009	11h43m48.62s	+19d58m12.1s	2010-02-22	35415296

Galaxy (1)	Program ID (2)	RA (J2000) (3)	Dec (J2000) (4)	Start time (5)	AORKEY (6)
NGC 3998	69	11h57m56.00s	+55d27m11.0s	2004-04-21	4452608
	80025	11h56m50.09s	+55d23m14.7s	2012-06-15	42242560
	80025	11h56m50.09s	+55d23m14.7s	2012-06-16	42242816
NGC 4026	30318	11h59m25.19s	+50d57m42.1s	2006-12-26	18034176
	80025	11h59m25.19s	+50d57m42.1s	2012-03-09	42247168
	80025	11h59m25.19s	+50d57m42.1s	2012-03-09	42247424
	80025	11h59m25.19s	+50d57m42.1s	2013-03-11	45629952
	80025	11h59m25.19s	+50d57m42.1s	2013-03-11	45630208
NGC 4151	3269	12h10m32.58s	+39d24m20.6s	2004-12-17	12463872
	61068	12h10m32.70s	+39d24m20.7s	2011-01-20	41200640
	61068	12h10m32.70s	+39d24m20.7s	2011-02-20	41214976
	80025	12h10m32.58s	+39d24m20.6s	2012-08-11	42253312
	80025	12h10m32.58s	+39d24m20.6s	2012-08-13	42253568
NGC 4261	69	12h19m22.70s	+5d49m35.0s	2004-05-27	4461056
NGC 4291	30603	12h21m43.87s	+75d19m21.3s	2007-02-19	18598144
NGC 4342	61062	12h23m38.70s	+6d57m14.1s	2011-03-13	30850560
	61062	12h23m48.50s	+7d11m12.9s	2010-07-31	30902528
NGC 4388	20695	12h25m43.11s	+12d43m06.6s	2006-07-06	14988288
	50763	12h25m46.75s	+12d39m43.5s	2008-07-15	27090688
	60173	12h26m38.70s	+13d13m55.4s	2010-03-10	35324160
	61068	12h25m46.80s	+12d39m43.1s	2011-03-16	41207552
	61068	12h25m46.80s	+12d39m43.1s	2011-07-21	41210624
NGC 4459	3649	12h29m00.03s	+13d58m42.8s	2005-01-22	11378944
NGC 4473	3649	12h29m48.87s	+13d25m45.7s	2005-01-22	11377920
NGC 4564	20371	12h36m26.99s	+11d26m21.5s	2006-02-09	14572032
NGC 4596	3674	12h39m55.94s	+10d10m33.9s	2005-06-10	11519232
NGC 4697	3403	12h48m35.91s	-5d48m03.1s	2005-07-16	10896896
NGC 4889	25	12h59m48.70s	+27d58m50.0s	2003-12-18	3859456
	25	12h59m48.70s	+27d58m50.0s	2004-07-04	3859968
NGC 4945	20256	13h04m44.06s	-49d33m59.8s	2005-07-22	14467840
	20256	13h04m44.06s	-49d33m59.8s	2006-02-12	14468608
	30292	13h04m44.06s	-49d33m59.8s	2006-08-08	17967104
	30292	13h04m44.06s	-49d33m59.8s	2007-02-20	17967360
	40410	13h05m27.48s	-49d28m05.6s	2007-08-07	21999616
	80239	13h05m11.09s	-49d31m27.1s	2012-03-26	45255936
NGC 5077	69	13h19m31.65s	-12d39m25.9s	2004-01-18	4478976
NGC 5128	50795	13h25m43.00s	-42d57m40.0s	2008-08-23	26922240
	61002	13h25m10.53s	-42d58m34.7s	2011-04-12	31529216
	61002	13h25m10.53s	-42d58m34.7s	2011-04-24	31528704
	61002	13h25m10.53s	-42d58m34.7s	2011-04-12	31529216
	61002	13h25m10.53s	-42d58m34.7s	2011-04-05	31529728
	61002	13h25m10.53s	-42d58m34.7s	2011-03-26	31530240
	61002	13h25m10.53s	-42d58m34.7s	2010-04-16	31530752
	61002	13h25m10.53s	-42d58m34.7s	2010-04-04	31531520
	61002	13h25m10.53s	-42d58m34.7s	2010-03-25	31532288
	61002	13h25m10.53s	-42d58m34.7s	2010-03-17	31533056
	60132	13h27m21.23s	-42d40m37.7s	2009-08-31	34870016
	101	13h25m27.62s	-43d01m08.8s	2004-02-10	4939008
NGC 5576	3403	14h21m03.68s	+3d16m15.6s	2005-07-15	10897408
NGC 5813	69	15h01m11.10s	+1d42m08.0s	2004-02-17	4490496
NGC 5845	20371	15h06m00.78s	+1d38m01.7s	2005-08-23	14572544
NGC 5846	20140	15h06m29.29s	+1d36m20.2s	2006-02-13	16310272
	69	15h06m29.20s	+1d36m20.0s	2004-03-08	4491264
NGC 6251	3418	16h32m31.97s	+82d32m16.5s	2004-12-16	10924288
NGC 7052	30877	21h18m33.05s	+26d26m48.7s	2006-11-26	19168000
NGC 7582	3269	23h18m23.50s	-42d22m14.0s	2004-11-27	12478720
	61068	23h18m22.90s	-42d22m11.0s	2011-01-08	41199616
	61068	23h18m22.90s	-42d22m11.0s	2011-07-19	41208832
NGC 7619	30318	23h20m14.52s	+8d12m22.5s	2006-12-25	18037760
NGC 7768	61009	23h50m58.93s	+27d13m41.8s	2010-01-16	35345408
UGC 03789	61009	7h19m30.92s	+59d21m18.4s	2009-11-10	36023296

the *overlap* correction, which successfully removed the “chessboard” pattern (see Figure 1 for an example).

#### 2.1.4. Sigma mosaics

For each individual cBCD frame, the IRAC Level 1 pipeline calculates the uncertainty associated to each pixel and produces an uncertainty frame (or sigma frame). The initial uncertainty is estimated as the Poisson noise in electrons plus the readout noise added in quadrature ( $\sigma^2 = \sigma_{\text{readoutnoise}}^2 + \sigma_{\text{Poisson}}^2$ ). This initial sigma frame is carried through the pipeline, and additional uncertainties (e.g. dark current and flat field un-

certainties) are added in quadrature when appropriate. When MOPEX generates an image mosaic, it also produces the associated sigma mosaic by interpolating the individual uncertainty frames and co-adding them, following the standard assumption of additive variances.

#### 2.1.5. Sky subtraction

Sky subtraction was performed manually on the image mosaics using the tasks *marksky* and *skyfit* of the IRAF<sup>4</sup> package GALPHOT<sup>5</sup>. The task *skyfit* also pro-

<sup>4</sup> IRAF is the Image Reduction and Analysis Facility, distributed by the National Optical Astronomy Observatory, which is oper-

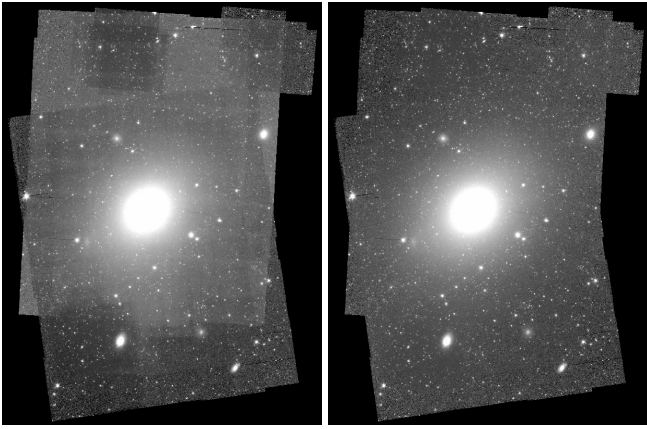


FIG. 1.— Example of the *overlap* correction. The image mosaic of the galaxy M49 was obtained by co-adding frames coming from 8 different AORs. The evident patchiness (left image) was removed (right image) using the *overlap* module.

vided an estimate of the sky root mean square ( $RMS_{\text{sky}}$ ).

#### 2.1.6. Additional aesthetic corrections

The image mosaics of 4 galaxies (NGC 0821, NGC 2974, NGC 4291, NGC 4459) were found to be affected by bright, highly saturated stars lying close to the target galaxies. These stars were modeled and subtracted using the software Galfit (Peng et al. 2010) and the extended IRAC Point Response Function (PRF) image at  $3.6\ \mu\text{m}$ . This helped remove the extended wings and spikes of the saturated stars (see Figure 2 for an example).

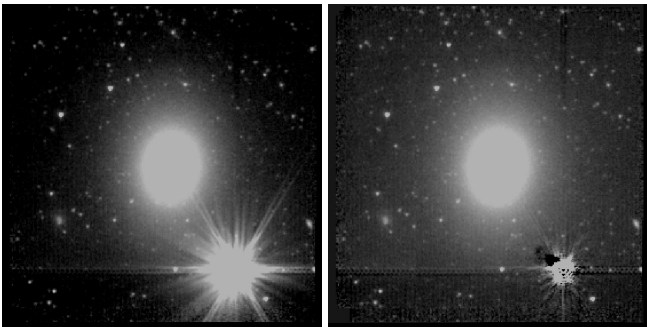


FIG. 2.— Example of aesthetic correction. The images show the mosaic of the galaxy NGC 4459 before (left) and after (right) the partial removal of a bright saturated star.

#### 2.1.7. Image masking

Galactic stars and any other objects different from the target galaxy were masked through a two-step procedure. First, we created an initial mask using the IRAF task *objmasks* that identifies objects by threshold sigma detection. Then, we refined each mask by hand, using the software SAOImage DS9<sup>6</sup> in conjunction with the IRAF

ated by the Association of Universities for Research in Astronomy (AURA) under cooperative agreement with the National Science Foundation.

<sup>5</sup> GALPHOT was developed in the IRAF - STSDAS environment mainly by W. Freudling, J. Salzer, and M. P. Haynes (Haynes et al. 1999).

<sup>6</sup> SAOImage DS9 development has been made possible by funding from the Chandra X-ray Science Center (CXC) and the High Energy Astrophysics Science Archive Center (HEASARC).

task *mskregions*. We identified and carefully masked not only contaminating sources located in the field of the image mosaic, but also objects overlapping with the target galaxy, such as foreground stars, background galaxies, globular clusters or red giant stars.

#### 2.1.8. 1D PSF

A universal, average, one-dimensional Point Spread Function was characterized using the IRAF task *imexamine*. A nonlinear least squares (Moffat 1969) profile<sup>7</sup> of fixed center and zero background was fit to the (background subtracted) pixels of 20 bright stars, belonging to different image mosaics. The best-fit parameters of the 20 stars were then averaged together. Doing so, we obtained  $(\alpha, \beta) = (2''.38, 4.39)$  (see Appendix A for the analytical expressions of the Moffat function).

#### 2.1.9. 2D PSF

The IRAC support team provides users with a two-dimensional instrument Point Response Function (PRF) at  $3.6\ \mu\text{m}$ . However, while this helped remove the extended wings of saturated stars (see Section 2.1.6), we found this PRF to be inadequate for the purposes of our modelling. In fact, the *FWHM* of the IRAC instrument PRF ( $\sim 1''.8$ ), as measured by the IRAF task *imexamine*, is systematically smaller than the average *FWHM* of “real” stars ( $\sim 2''.0$ ). Figure 3 illustrates this issue. We also tested the IRAC PRF by providing it as the input Point Spread Function (PSF) for Galfit and fitting a number of stars in different image mosaics. A visual inspection of the fit residuals confirmed that the IRAC instrument PRF is narrower than “real” point sources. For this reason, we constructed our 2D PSF according to the following method (as directed by C. Peng, private communication).

We provided the IRAC instrument PRF as the input PSF for Galfit and simultaneously fit 7 bright stars (belonging to different mosaics), modeling the stars with Moffat profiles and constraining all the profiles to have the same  $(\alpha, \beta)$ , position angle and axis ratio. The 2D PSF image was then obtained by taking the best fit Moffat model – the same best-fit model for all 7 stars, by construction – and convolving it with the IRAC instrument PRF. The advantage of this method is to obtain a 2D PSF that is wider than the instrument PRF, but maintains the asymmetric features of the instrument PRF (e.g. wings and spikes). We then tested this 2D PSF on a number of stars (these stars were different from the 7 stars employed to build the 2D PSF image) and verified that it correctly reproduces the shape of “real” point sources.

### 2.2. Additional data

#### 2.2.1. Kinematics

A kinematical classification (slow/fast rotator) is available for 34 of our 75 galaxies from the ATLAS<sup>3D</sup> survey (Emsellem et al. 2011) and for 3 additional galaxies

<sup>7</sup> The (Moffat 1969) profile has the following form:

$$\mu = \mu_0 - 2.5 \log \left[ 1 + \left( \frac{R}{\alpha} \right)^2 \right]^{-\beta}, \quad (1)$$

where  $R$  is the projected galaxy radius,  $\mu_0$  is the central surface brightness, and  $\alpha$  and  $\beta$  regulate the width and the shape of the profile.



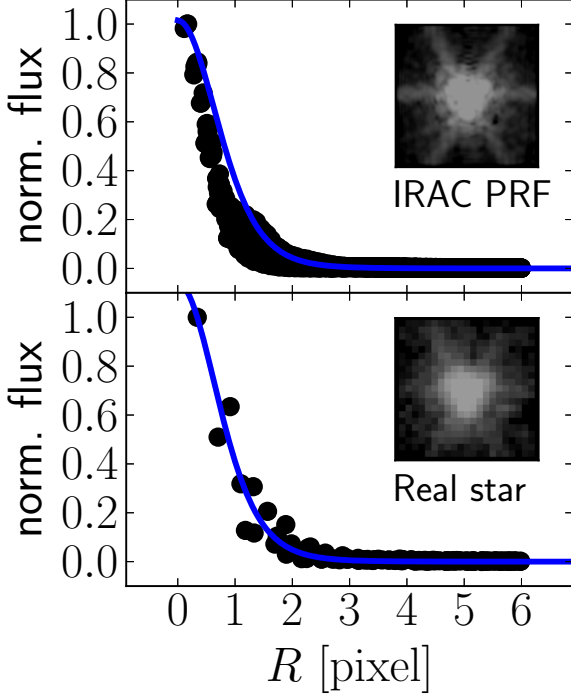


FIG. 3.— Normalized flux versus radial distance from the image centroid of an observed point source (bottom panel) and of the IRAC instrument Point Response Function (PRF, top panel). The normalized flux is given in arbitrary units, and the radial distance is in units of pixel size of the IRAC detector (1 pixel = 1'' .22). The blue solid line shows our 1D Moffat PSF model, which has been normalized to intersect the data point with the largest flux. The  $FWHM$  of the IRAC PRF is clearly smaller than that of a “real” star. The inserts display the images of the observed point source and the IRAC PRF.

from Scott et al. (2014). This classification (Table 1, column 7) concerns the kinematic properties of galaxies within the spectroscopic instrument’s field-of-view, but does not contain additional information – crucial for our analysis – about kinematic substructures, such as embedded disks or kinematically decoupled components, which can require separate modeling. For this reason, we also visually inspected the velocity fields of our galaxies, when available from the literature. Velocity maps were taken from the ATLAS<sup>3D</sup> survey for 34 galaxies (observed with SAURON by Krajnović et al. 2011), from Scott et al. (2014) for 2 galaxies (observed with WiFeS) and from the SLUGGS survey for 12 galaxies (observed with DEIMOS by Arnold et al. 2014). While the field-of-views of SAURON (33'' × 41'') and WiFeS (25'' × 38'') reach to about one galaxy effective radius (for our local galaxies), observations taken with DEIMOS can probe the galaxy kinematics well beyond two effective radii.

### 2.2.2. AGNs and nuclear dust

The X-ray, UV and optical radiation emitted by the accretion disks of Active Galactic Nuclei (AGNs) can stimulate infrared thermal emission from circumnuclear dust, if present. This means that if a galaxy hosts an optical AGN *and* a certain amount of nuclear dust, we may detect some non-stellar nuclear emission at 3.6  $\mu\text{m}$ . It is therefore important to identify which of our galaxies have both an optical AGN and circumnuclear dust. To

help with this task, we searched NED<sup>8</sup> for the individual galaxies and their associated literature. Unsurprisingly, dusty AGNs were more frequently found in late-type spiral galaxies, and modelled by us with either a point source or a PSF-convolved Gaussian.

### 2.2.3. Sérsic/core-Sérsic classification

Core-Sérsic galaxies (Graham & Guzmán 2003; Graham et al. 2003; Trujillo et al. 2004) are galaxies (or bulges) with partially depleted cores, i.e. a central deficit of light relative to the inward extrapolation of their outer Sérsic light profile. Such deficits were first noted and researched by King & Minkowski (1966). Sérsic galaxies, instead, do not exhibit such central stellar deficits. Partially depleted cores, as measured from high-resolution observations, have typical sizes of a few tens of parsecs (Dullo & Graham 2013; Rusli et al. 2013a). The majority are thus unresolved in our image mosaics. We masked these unresolved cores (identified in high-resolution images, see Table 1) by excluding the surface brightness profile within 3 PSF’s  $FWHM$  from the galaxy center. In case of cores with sizes exceeding the PSF’s  $FWHM$ , we excluded the data points within the size of the core plus 3 PSF’s  $FWHM$ . The Sérsic/core-Sérsic classification presented in this work (Table 1, column 5) comes from the compilation of Savorgnan & Graham (2014), who identified partially depleted cores according to the same criteria used by Graham & Scott (2013). When no high-resolution image analysis was available from the literature, they inferred the presence of a partially depleted core based on the stellar velocity dispersion,  $\sigma$ : a galaxy is classified as core-Sérsic if  $\sigma > 270 \text{ km s}^{-1}$ , or as Sérsic if  $\sigma < 166 \text{ km s}^{-1}$ . This resulted in us assigning cores to just 2 galaxies using this alternative method when no high resolution image was available.

## 3. ANALYSIS

### 3.1. Isophotal analysis

We performed an isophotal analysis of our galaxies using the IRAF task `ellipse` (Jedrzejewski 1987), which fits elliptical isophotes to galaxy images. The center of the isophotes was held fixed, while the ellipticity ( $\epsilon$ ), the position angle ( $P.A.$ ), and the amplitude of the fourth harmonic<sup>9</sup> ( $B_4$ ) were allowed to vary with radius. The step in semi-major axis length between successive ellipses was first set to increase linearly, and then geometrically in our second run<sup>10</sup>. As a result, for each galaxy we produced respectively a “linearly sampled” and a “logarithmically sampled” surface brightness profile along the major-axis. Major-axis surface brightness profiles were additionally converted into the equivalent-axis, i.e. the geometric mean of the major ( $a$ ) and minor ( $b$ ) axis ( $R_{\text{eq}} = \sqrt{ab}$ ), equivalent to the circularized radius. This resulted in 4 profiles per galaxy. Isophotes corresponding to an intensity less than three times the root mean square

<sup>8</sup> NED is the NASA/IPAC Extragalactic Database.

<sup>9</sup> The amplitude of the fourth harmonic deviations from perfect ellipses ( $B_4$ ) parameterizes the diskyness ( $B_4 > 0$ ) or boxyness ( $B_4 < 0$ ) of the isophotes.

<sup>10</sup> In the case of linear steps, the semi-major axis length for the next ellipse was calculated by adding 1 pixel to the current length. In the case of geometric steps, the semi-major axis length for the next ellipse was calculated as 1.1 times the current length.

of the sky background fluctuations ( $3 \times RMS_{\text{sky}}$ ) were ignored. Some surface brightness profiles were truncated at our discretion before the  $3 \times RMS_{\text{sky}}$  limit, according to specific technical reasons (e.g. contamination from light of a neighboring galaxy, disturbed morphology in the galaxy outskirts, etc.). Individual cases are discussed in Section ??.

### 3.2. Unsharp masking

Unsharp masking is an image sharpening technique that is useful to reveal asymmetric structures in galaxies, such as bars or (inclined) embedded disks. First, the original galaxy image was smoothed with a Gaussian filter. Then, the original image was divided by the smoothed one. The result of such an operation is the “unsharp mask”. The asymmetric features revealed by this technique have sizes comparable to the  $FWHM$  of the Gaussian kernel used for the smoothing. Therefore, for each galaxy, we produced a set of different unsharp masks by varying the  $FWHM$  of the filter, to identify all the asymmetric features that could bias the fitting process and may therefore need to be considered during the galaxy modelling phase. This information was used in combination with kinematic and AGN information discussed in Section 2.2.

### 3.3. 1D fitting routine

The decomposition of the surface brightness profiles was performed with software written by G. Savorgnan. This software can fit an observed surface brightness profile with any linear combination of a set of analytical functions (Sérsic, exponential, Gaussian, Moffat, Ferrer, symmetric Gaussian ring etc. see Appendix A for a description of the analytical form of these profiles). At each iteration, the model is numerically convolved with a Moffat filter, to account for PSF effects, and then matched to the data. The minimization routine is based on the Levenberg-Marquardt algorithm. During the fit, we deliberately did not make use of any weighting scheme on the data points that constitute the surface brightness profile, although the use of a linearly and logarithmically sampled profile effectively represents a different weighting scheme. The all too often over-looked ?? with (signal-to-noise)-based weighting schemes is that they immediately become an incorrectly biased weighting schemes when additional components are present but not modelled. For example, fitting a Sérsic model to what is actually a nucleated elliptical galaxy immediately ?? a (signal-to-noise)-based weighting scheme and results in Sérsic parameters which describe the bulge less accurately than had no (signal-to-noise)-weighting been used. While we have paid careful attention to the components in each galaxy, and more so than the studies upon which our work is building from, this is an issue that warrants the non application of (signal-to-noise)-based weighting schemes. What is best in theory is not always best in practice – in this case, because theory does not allow for unknown additional components that are modelled.

### 3.4. Smoothing technique

Some nearby galaxies in our sample have very large apparent sizes and for them we obtained surface brightness profiles more extended than 8 arcmin. This means that

their outermost (significant) isophote corresponds to a projected galactic radius  $R$  of more than 240 times the  $FWHM$  of the instrumental PSF. Such level of spatial resolution is unnecessary for the purposes of our analysis and, especially in the case of a clumpy star forming galaxy, it results in a “noisy” surface brightness profile. Moreover, in the case of a linearly sampled light profile, it significantly prolongs the computational time of the fitting routine (because, at each iteration, the PSF convolution is performed numerically on a large array). To overcome this problem, we introduced a method to which we refer as the “smoothing technique”. This method was applied to the galaxies M31, M81, NGC 4945 and NGC 5128. For each of these galaxies, we took the image mosaic and we convolved it with a Gaussian filter whose  $FWHM$  was larger than the  $FWHM$  of the instrumental PSF. We then ran `ellipse` on the convolved image and extracted “linearly sampled” and “logarithmically sampled” surface brightness profiles. For the “linearly sampled” profiles, we set the radial step between contiguous isophotes to be comparable to the  $FWHM$  of the smoothing Gaussian filter. Doing so, we reduced the number of fitted isophotes and we also produced smoother surface brightness profiles. Before the software fit a smoothed light profile, the model to be fit was convolved twice: the first time to account for PSF effects, and the second time to account for the artificial Gaussian smoothing applied to the image mosaic.

### 3.5. Identifying and modeling sub-components

In this Section we give a general overview of the guidelines that we followed to identify and model the sub-components that constitute our galaxies. However, given the level of accuracy and detail to which each galaxy decomposition has been performed in our analysis, it is hard to encompass all aspects of this matter in a few paragraphs. The modeling of each galaxy represented a particular and original problem, and we remand the reader to Section ??, where we provide individual descriptions of the galaxies that we analyzed.

As stressed in Section 1, our investigation is primarily focused on the central spheroidal components of galaxies. We assumed *a priori* that each of our galaxies has a unique spheroidal component, that we modeled with a Sérsic profile.

Disks were usually fit with the exponential model, although in the case of highly inclined or edge-on systems we preferred using an  $n < 1$  Sérsic function. Pastrav et al. (2013a,b) showed that, due to projection effects, their simulated images of inclined galaxy disks are better fit by a Sérsic function with  $n < 1$  than by a pure exponential model. The inclined, embedded disks of some “elliptical” galaxies were described with Ferrer functions, rather than a  $n < 1$  Sérsic function. This choice was partly motivated by the fact that a Sérsic + Ferrer model is less degenerate than a Sérsic + Sérsic model, since the Sérsic profile can assume any concave ( $n > 1$ ) or convex ( $n < 1$ ) curvature, whereas the Ferrer profile can only have a negative curvature as required for an inclined disk. The presence of large-scale disks, such as those of lenticular and spiral galaxies, were known *a priori* from the galaxy morphological classification (as listed on NED), although some of them were re-classified by us as having intermediate-scale embedded disks. These were identi-

fied in a number of different ways. If highly inclined, they can obviously be spotted from the galaxy image or the unsharp mask. Local maxima in the ellipticity and fourth harmonic profiles can provide footprints of less obvious embedded disks. In particular, the ellipticity profile helps distinguish embedded disks from large-scale disks. Galaxy disks typically have fixed ellipticity, reflecting their inclination to our line of sight. On the other hand, spheroids can have their ellipticities varying with radius, but they are usually rounder than inclined disks, thus their average ellipticities are lower than those of inclined disks. If the ellipticity profile of a galaxy increases with radius, this can be ascribed to an inclined disk that becomes progressively more important over the spheroid, whereas a radial decrease of ellipticity signifies the opposite case. Therefore, in a situation where a disk is identified from the galaxy image, but its extent (large- or intermediate-scale) is ambiguous, the shape of the ellipticity profile can be decisive. Another way to establish the presence of an embedded disk is to look at the velocity map of a galaxy, following the approach of Arnold et al. (2014). A local angular momentum decrease with increasing radius is indicative of an intermediate-scale disk that fades toward larger radii.

Bars are usually recognizable from galaxy images and unsharp masks, although local maxima/minima or abrupt changes in the radial profiles of the isophotal parameters can provide additional evidence for less obvious bars. As noted, we were able to successfully fit bars with a Ferrer function or a low- $n$  Sérsic model ( $n \sim 0.2$ ).

The presence of a nuclear component – either resolved or unresolved – was generally expected in (but not restricted to) galaxies that host an optical AGN and circumnuclear dust. Nuclear stellar disks and nuclear star clusters fall into the category of nuclear components too, but their identification can be more subtle than for AGNs. Nuclear clusters have typical sizes of a few parsecs, therefore for the majority of our galaxies they are unresolved in *Spitzer*/IRAC 3.6  $\mu\text{m}$  observations. If an identification from high-resolution observations was available from the literature, we relied on that, otherwise we concluded that a galaxy was nucleated from an excess of nuclear light in the residuals of the fit<sup>11</sup>. Unresolved nuclear components were fit with our optimal Moffat PSF, whereas resolved nuclear components were modeled with (PSF-convolved) narrow Gaussian functions.

Rings were identified from galaxy images and unsharp masks, and modeled with symmetric Gaussian ring profiles.

As an illustration, we consider the galaxy NGC 2974, a spiral galaxy which has been misclassified as an elliptical galaxy in the RC3 catalog (de Vaucouleurs et al. 1991). This galaxy hosts a Seyfert AGN (Véron-Cetty & Véron 2006) and filamentary dust in its center (Tran

et al. 2001). NGC 2974 is classified as a fast rotator by the ATLAS<sup>3D</sup> survey, and indeed the velocity map obtained by the SLUGGS survey shows that the galaxy kinematics is rotation-dominated well beyond three effective radii ( $R > 150''$ ), as expected from a large-scale disk. From an inspection of the unsharp mask, we identified a ring at  $R \sim 50''$ , which might be a residual of two tightly wound spiral arms, and an elongated bar-like component within  $R \lesssim 30''$ , that is in addition to the more spherical bulge and produces a peak in the ellipticity and position angle profiles at  $R \sim 20''$ . Our 1D galaxy decomposition for NGC 2974 (Figure 4) consists of a Sérsic bulge, an exponential large-scale disk, a Ferrer bar, a Gaussian nuclear component (AGN) and a Gaussian ring. Although the ring is extremely faint, it is important to account for it in the galaxy decomposition. A model without the ring component results in a “steeper” exponential profile for the disk (i.e. the exponential model has a smaller scale length and a brighter central surface brightness) and produces bad residual structures within  $R \lesssim 40''$ . Our best-fit model returns a 3.6  $\mu\text{m}$  bulge major-axis effective radius  $R_{\text{e,sph}}^{\text{maj}} = 8.3$  arcsec, equivalent-axis Sérsic index  $n_{\text{sph}}^{\text{eq}} = 1.2$  and apparent magnitude  $m_{\text{sph}} = 8.65$  mag. Sani et al. (2011) modeled NGC 2974 with a Sérsic bulge and a Gaussian nuclear component (AGN), but did not account for the large-scale disk. From their best-fit 2D model, they obtained a three times larger 3.6  $\mu\text{m}$  bulge major-axis effective radius ( $R_{\text{e,sph}}^{\text{maj}} = 27.2$  arcsec), a 2.5 times larger Sérsic index ( $n_{\text{sph}} = 3$ ), and a significantly brighter apparent magnitude ( $m_{\text{sph}} = 7.28$  mag).

### 3.6. 2D fits

Two-dimensional decompositions were carried out using the software IMFIT (Erwin 2015). For each galaxy, we built a 2D model that was consistent with the corresponding 1D model in terms of number and type of components. Because the Ferrer profile is not made available in IMFIT, bars were fit with a 2D Gaussian function. The 2D decomposition of NGC 2974 is presented in Figure 5. The galaxy was modeled with a Sérsic bulge, an exponential disk and a Gaussian bar. The nuclear component was masked and the ring was not modeled<sup>12</sup>. Our best-fit 2D model returns a bulge major-axis effective radius  $R_{\text{e,sph}}^{\text{maj}} = 10.5$  arcsec, a bulge Sérsic index  $n_{\text{sph}} = 1.3$  and a 3.6  $\mu\text{m}$  bulge apparent magnitude  $m_{\text{sph}} = 8.39$  mag, in fairly good agreement with our 1D decomposition. Fits and descriptions for the other galaxies are available online.

## 4. RESULTS

For each galaxy, after we identified its various components and built a model accordingly, we simultaneously performed a set of four 1D fits. All four fits use a Moffat-convolved model. Two fits use the major-axis surface brightness profile and the remaining two use the equivalent-axis surface brightness profile. For each of these pairs, we use a logarithmically sampled surface

<sup>11</sup> This conclusion was drawn after going through the following steps. First we identified all the sub-components of a galaxy (assuming that the galaxy was not nucleated), built a model accordingly and fit it to the data. If the residuals of the fit showed a nuclear light excess, we repeated the fit by excluding the data points within the nuclear region. Only after checking that the outcome of the last fit was consistent with a fit that included a small nuclear component, we inferred the presence of a stellar nuclear component.

<sup>12</sup> We built the 2D model first including and then omitting a gaussian ring component, but both models converged to the same solution, i.e. the fit “ignored” the presence of the faint ring. This did not happen in the 1D decomposition because of the different weighting scheme used by the fitting routines.

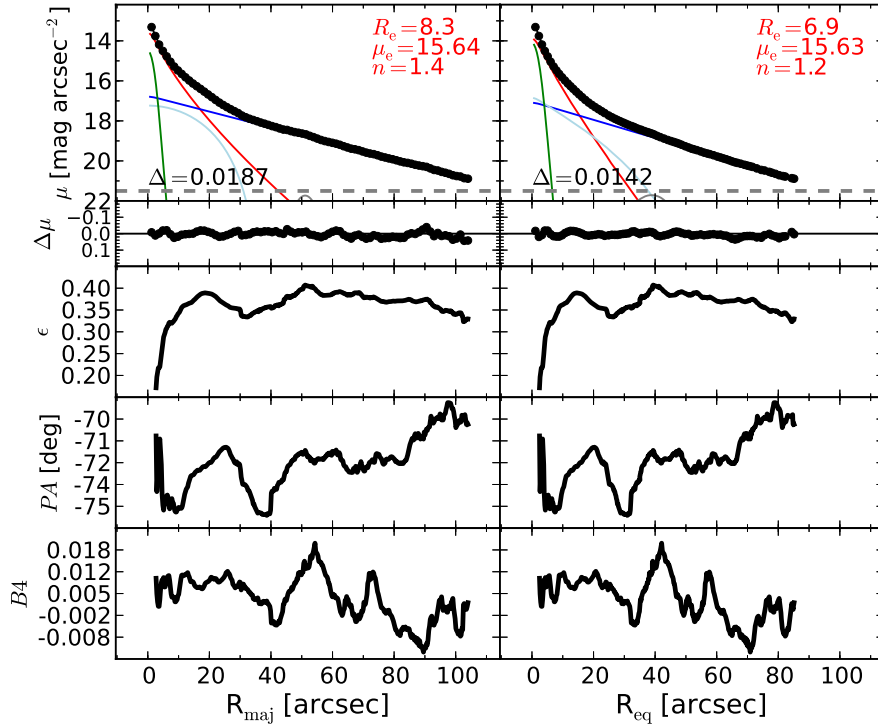


FIG. 4.— Best-fit model and isophotal parameters for the galaxy NGC 2974. The left panels refer to the major-axis  $R_{\text{maj}}$ , whereas the right panels refer to the equivalent-axis  $R_{\text{eq}}$ . The top panels display the galaxy surface brightness radial profiles obtained with a linear sampling. The black points are the observed data. The color lines represent the individual (PSF-convolved) model components: red=Sérsic (bulge), blue=exponential (disk), green=Gaussian (AGN), cyan=Ferrer (bar), gray=Gaussian ring (ring). The best-fit parameters for the Sérsic profile are included. The total (PSF-convolved) model is shown with a black dashed line, but it is hard to distinguish because it almost perfectly matches the data. The horizontal grey dashed line indicates the  $3 \text{ RMS}_{\text{sky}}$  level.  $\Delta$  denotes the rms scatter of the fit in units of  $\text{mag arcsec}^{-2}$ .  $\Delta\mu$  are the residuals from the fit. The six panels below show the ellipticity ( $\epsilon$ ), position angle ( $PA$ ) and fourth harmonic ( $B4$ ) radial profiles.

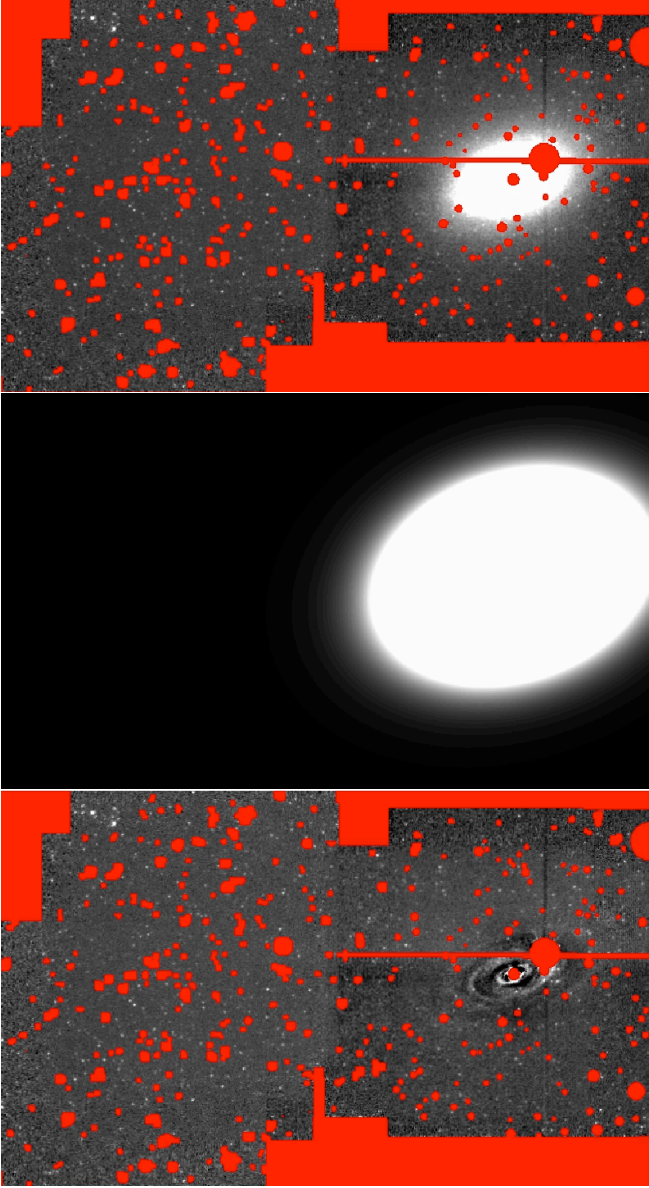


FIG. 5.— The image of the galaxy NGC 2974 with its mask (top panel), the best-fit 2D model (middle panel), and the residual image after the subtraction of the 2D model (bottom panel). The ring has not been modeled, and therefore appears in the residual image.

brightness profile and a linearly sampled surface brightness profile. Because our fitting routine intentionally does not employ an error weighting scheme on the data points that constitute the surface brightness profile, a fit to a logarithmically sampled profile puts more weight on the inner region of the galaxy and poorly constrains the outskirts. On the other hand, a fit to a linearly sampled surface brightness profile equally treats inner and outer regions, but is more susceptible to sky-background subtraction issues.

We found that the fits are, in general, more sensitive to the choice of the initial parameters when using logarithmically sampled profiles than linearly sampled profiles. In addition, a visual examination of the residuals revealed that the quality of the fit within one galaxy

effective radius is superior when tighter constraints are put on the galaxy outskirts. In other words, the better quality of the residuals led us to prefer the fits that use linearly sampled surface brightness profiles, although the results were usually very similar, as might be expected. Among the initial sample of 75 galaxies, we did not attempt to model 3 galaxies: M32, NGC 4486A and the Circinus Galaxy. The first two... **AL: can you write a short sentence about these 2 galaxies, that have uncertain morphology, because they have been stripped, blah blah, maybe put one reference? please and thank you.** The Circinus Galaxy lies at only 4 degrees from the Galactic Plane, therefore its image mosaic is contaminated by a large number of foreground stars. Of the remaining 72 galaxies, we obtained satisfactory 1D decompositions for 66, whereas the models of 6 galaxies were judged not reliable and were thus excluded. We also performed reliable 2D decompositions for 31 galaxies.

A galaxy-by-galaxy comparison between our best-fit models and those from the previous literature helped identify the optimal decompositions and past problems. We compared our best-fit models with those of Graham & Driver (2007a), Sani et al. (2011), Beifiori et al. (2012), Vika et al. (2012) and Läscher et al. (2014a). We also considered the best-fit models of Laurikainen et al. (2010) and Rusli et al. (2013a) because, although they did not specifically deal with black hole – galaxy scaling relations, their galaxy samples significantly overlap with ours.

Table 3 lists the results from both the 1D and 2D fits.

#### 4.1. 1D versus 2D decompositions

How do 1D and 2D decompositions compare with each other? Although an exhaustive analysis is beyond the scope of the present work, we believe that some of the readers might be interested in our practical knowledge, having dealt with 1D and 2D techniques of galaxy modeling at the same time.

We summarize our experience in the following points:

- A visual inspection of galaxy images and their unsharp masks is often not sufficient to accurately identify all galaxy components. Embedded disks or weak bars can easily be missed, and (inclined) intermediate-scale disks can be confused with large-scale ones. In this regards, the 1D isophotal analysis is extremely helpful. Local minima/maxima or abrupt changes in the ellipticity, position angle and fourth harmonic profiles contain precious information about the galaxy constituents.
- The ellipticity and position angle of bulges can vary with radius. The analytic functions used by 2D decomposition codes to fit galaxy components have fixed ellipticity and position angle, thus they cannot account for their radial gradients. This problem is overcome with 1D decomposition techniques.
- The interpretation of the residuals is often crucial to identify the optimal decomposition for a galaxy. In our experience, we found that the reading of 1D residuals was easier than that of 2D residuals.





Galaxy (1)	1D Major-axis			1D Equivalent-axis					Q.F. (10)	2D		
	$R_e$ (2)	$\mu_e$ (3)	$n$ (4)	$R_e$ (5)	$\mu_e$ (6)	$n$ (7)	$m_{\text{sph}}$ (8)	$m_{\text{gal}}$ (9)		$R_e$ (11)	$n$ (12)	$m_{\text{sph}}$ (13)
NGC 5845	3.6	14.79	2.5	3.1	14.64	2.3	9.05	8.91	3	2.8	2.4	9.09
NGC 5846	105.1	19.67	6.4	83.4	19.28	5.7	6.10	6.10	2	85.1	5.2	6.14
NGC 6251	41.7	19.82	6.8	30.1	19.31	5.6	8.35	8.35	1	39.3	7.1	8.27
NGC 7052	59.4	19.38	4.2	37.0	19.19	5.6	7.79	7.79	1	36.2	4.0	8.09
NGC 7582	—	—	—	—	—	—	—	—	—	—	—	—
NGC 7619	63.2	19.53	5.3	58.0	19.55	5.2	7.21	7.15	2	—	—	—
NGC 7768	92.9	21.37	8.4	42.1	20.15	6.7	8.36	8.36	2	—	—	—
UGC 03789	1.8	15.26	1.9	2.4	15.39	1.4	10.65	9.22	3	—	—	—

Although we attempted 2D modeling for all galaxies in our sample, nearly half of the 2D decompositions were not successful or did not converge. For the 31 galaxies that had successful 1D and 2D decompositions, we compare their 1D and 2D best-fit parameters in Figures 6, 7 and 8. The agreement between 1D and 2D effective radii and magnitudes is remarkable, whereas a larger amount of scatter in the Sérsic indices plot might be caused by the fact that 2D measurements do not exactly correspond to 1D equivalent-axis measurements. No systematic effects are observed in any of these three plots, which indicates that 1D and 2D techniques of galaxy modeling – when performed on the same galaxy – give consistent results. In conclusion, since we found that the best-fit parameters do not depend on the decomposition method (1D or 2D) used, but we obtained more successful 1D decompositions than 2D, we will base our analysis only on the results from 1D fits.

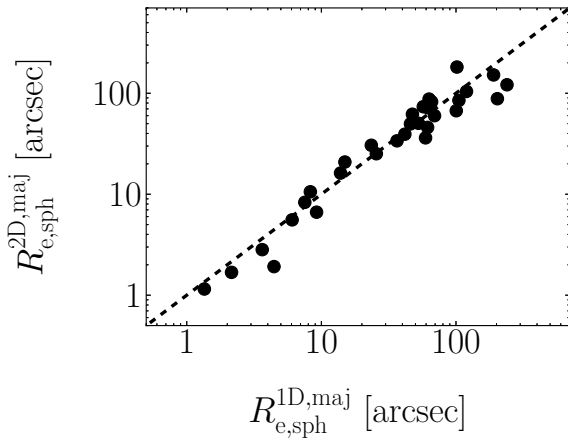


FIG. 6.— 2D versus 1D major-axis measurements of effective radii. The dashed line displays the 1:1 relation.

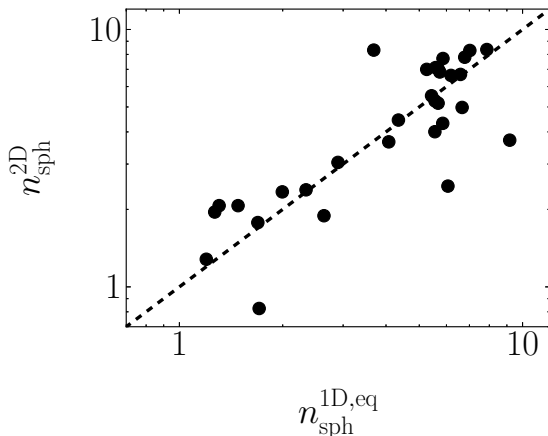


FIG. 7.— 2D measurements of Sérsic indices can be approximated to 1D equivalent-axis measurements, and are therefore compared to them in this plot. The dashed line displays the 1:1 relation.

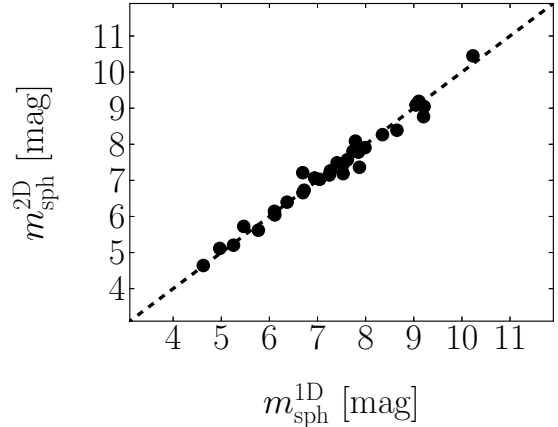


FIG. 8.— 2D versus 1D measurements of  $3.6 \mu\text{m}$  bulge magnitudes. The dashed line displays the 1:1 relation.

#### 4.2. Parameter uncertainty

Estimating the uncertainties associated with the best-fit parameters of our 1D galaxy decompositions is not straightforward. Monte Carlo simulations could be used for this purpose, but they would take into account only random errors and not unknown systematic ones. Systematic errors include incorrect sky subtraction, inaccurate masking of contaminating sources, imprecise description of the PSF, erroneous choice of model components (for example, when failing to identify a galaxy sub-component and thus omitting it in the model, or when describing a galaxy sub-component with an inadequate function), the radial extent of the surface brightness profile and its sampling. When performing multi-component decomposition of high signal-to-noise images of nearby – therefore well resolved – galaxies, errors are dominated by systematics rather than Poisson noise. For this reason, we decided to estimate the uncertainties of the bulge best-fit parameters with a method that took into account systematic errors.

##### 4.2.1. Goodness of the bulge modeling

To do this, we first had to evaluate the goodness of the modeling of the bulge component. For each of our fits, we calculated the associated *RMS* scatter<sup>13</sup>. Although useful to evaluate the overall quality of a galaxy decomposition, the *RMS* scatter alone cannot be used to assess the goodness of the fit for the spheroidal component only, unless the galaxy is a pure spheroid and has consequently been modeled with a single Sérsic profile. To illustrate this point with an example, one can imagine a situation in which a galaxy is thought to be made of a small bulge and a much more extended disk. This galaxy is decomposed with a Sérsic + exponential

<sup>13</sup> The *RMS* scatter of a fit was computed as:

$$\Delta = \sqrt{\frac{\sum_{i=0}^N (\mu_i^{\text{observed}} - \mu_i^{\text{model}})^2}{N_{\text{DOF}}}}, \quad (2)$$

where  $N_{\text{DOF}}$  is the number of degrees-of-freedom,  $\mu^{\text{observed}}$  is the observed surface brightness and  $\mu^{\text{model}}$  is the model surface brightness.



model. The exponential function provides an excellent description of the light profile of the disk, whereas the Sérsic function does not do the same for the bulge. The residuals of the fit will then be flat and close to zero at large radii, where the emission of the disk dominates over that of the bulge, while they will display significant structures at small radii, in correspondence of the poorly fit spheroidal component. In case of linear sampling, because the part of the surface brightness profile pertaining to the disk contains more data points than the part pertaining to the bulge, the global *RMS* scatter will be relatively small, but it obviously will not reflect the accuracy of the fit to the spheroidal component only.

A simple but powerful way to get a feeling of how precisely the global model describes the spheroidal component is to look at the major- and equivalent-axis fits of each galaxy and visually inspect the structures of the residuals within  $\sim 1 - 2$  bulge effective radii. We did this using a grade from 1 to 3, assigned according to the following criteria.

- 1) A grade of 1 was given to the best fits, i.e. fits that do not exhibit any of the problems listed below.
- 2) A grade of 2 was used in the following cases: the residuals in correspondence of the bulge component are not randomly distributed around zero, being symptomatic of a Sérsic model having a curvature (regulated by the Sérsic index  $n$ ) that does not match the real “shape” of the bulge; when we identified, but were not able to accurately model a galaxy sub-component; in the case of significant inconsistencies between the model and the observed galaxy properties (e.g. an embedded disk modeled with an exponential function, whose scale length does not match the size of the disk as expected from the ellipticity profile or the velocity map); when the Sérsic profile used to describe the bulge component has a size – as measured by the effective radius – comparable to a few times the *FWHM* of the PSF.
- 3) A grade of 3 was assigned to the poorer and more anomalous fits, or those affected by an obvious degeneracy between the bulge Sérsic profile and the remaining model components (e.g. when the bulge Sérsic index varies for more than 50% **TBD: how often what?** among the four different realizations of the fit, or when the output of the fit strongly depends on the choice of the initial parameters).

As a result, we classified 27 galaxies (38% of the 72 galaxies for which we attempted a 1D decomposition) with grade 1, 29 galaxies (40%) with grade 2 and 10 galaxies (14%) with grade 3.

#### 4.2.2. Uncertainties on $n_{\text{sph}}$

In Figure 9, for 58 galaxies, we compare the measurements of the bulge Sérsic index obtained by different authors with those obtained by us. For each galaxy, we computed the average value  $\langle \log(n_{\text{sph}}) \rangle$  of all the available measurements, and we plot it against the scatter of the individual measurements around  $\langle \log(n_{\text{sph}}) \rangle$ . The measurements are deliberately heterogeneous, in the sense that they were obtained from 1D or 2D decompositions of data in different wavelengths, and

they refer either to the major-axis or to the equivalent-axis. In Figure 9, the black histogram shows the distribution of the scatter around  $\langle \log(n_{\text{sph}}) \rangle$  only for our measurements. 38% of this distribution lie within  $-\sigma_1^- = -0.08$  dex and  $+\sigma_1^+ = +0.06$  dex, 78% lie within  $-\sigma_2^- = -0.21$  dex and  $+\sigma_2^+ = +0.17$  dex, and 92% lie within  $-\sigma_3^- = -0.25$  dex and  $+\sigma_3^+ = +0.25$  dex. We elect to use  $\pm\sigma_1^\pm$ ,  $\pm\sigma_2^\pm$  and  $\pm\sigma_3^\pm$  as  $1\sigma$  uncertainties for our measurements of  $\log(n_{\text{sph}})$  obtained from “grade 1”, “grade 2” and “grade 3” fits, respectively.

#### 4.2.3. Uncertainties on $R_{\text{e,sph}}$

The uncertainties on the bulge effective radii were computed with the same method used for the Sérsic indices. However, in Figure 10 we include only major-axis measurements of  $R_{\text{e,sph}}$ . The associated  $1\sigma$  uncertainties for our measurements of  $\log(R_{\text{e,sph}})$  are  $-\sigma_1^- = -0.11$  dex and  $+\sigma_1^+ = +0.07$  dex,  $-\sigma_2^- = -0.30$  dex and  $+\sigma_2^+ = +0.32$  dex, and  $-\sigma_3^- = -0.39$  dex and  $+\sigma_3^+ = +0.42$  dex.

#### 4.2.4. Uncertainties on $m_{\text{sph}}$

To estimate the uncertainties on the bulge magnitudes, we compared (see Figure 11) only measurements coming from *K*-band or  $3.6 \mu\text{m}$  observations.  $3.6 \mu\text{m}$  magnitudes were converted into *K*-band magnitudes by an additive factor of  $+0.27$  mag, which was estimated using the stellar population models of Worthey (1994), assuming a 13 Gyr old single-burst stellar population with solar metallicity. The associated  $1\sigma$  uncertainties for our measurements of  $m_{\text{sph}}$  are  $-\sigma_1^- = -0.11$  mag and  $+\sigma_1^+ = +0.18$  mag,  $-\sigma_2^- = -0.58$  mag and  $+\sigma_2^+ = +0.66$  mag, and  $-\sigma_3^- = -0.66$  mag and  $+\sigma_3^+ = +0.88$  mag.

**NOTE: When converting from K-band to 3.6, Galactic absorption was not taken into account!!!! But I have the feeling that it's not significant...**

#### 4.2.5. Uncertainties on $\mu_{\text{e,sph}}$

As for the bulge magnitudes, we estimated the uncertainties on the bulge effective surface brightnesses  $\mu_{\text{e,sph}}$  by comparing only *K*-band or  $3.6 \mu\text{m}$  measurements (see Figure 12), and accounting for the corrective factor. Because not explicitly reported by their authors, literature effective surface brightnesses were calculated by us as:

$$\mu_{\text{e,sph}} = m_{\text{sph}} + 5 \log \left( R_{\text{e,sph}}^{\text{maj}} \sqrt{(b/a)_{\text{sph}}} \right) + 2.5 \log \left[ 2\pi n_{\text{sph}} e^{b_n} b_n^{-2n_{\text{sph}}} \Gamma(2n_{\text{sph}}) \right], \quad (3)$$

where  $b_n$  and  $\Gamma(2n_{\text{sph}})$  are defined in Section A, and  $(b/a)_{\text{sph}}$  is the bulge axis ratio. While Laurikainen et al. (2010) and Sani et al. (2011) reported their estimates of  $(b/a)_{\text{sph}}$ , Vika et al. (2012) and Läscher et al. (2014a) did not. For the last two studies, we used the values of  $(b/a)_{\text{sph}}$  reported by Sani et al. (2011). The associated  $1\sigma$  uncertainties for our measurements of  $\mu_{\text{e,sph}}$  are  $-\sigma_1^- = -0.33$  mag and  $+\sigma_1^+ = +0.57$  mag,  $-\sigma_2^- = -0.84$  mag and  $+\sigma_2^+ = +1.59$  mag, and  $-\sigma_3^- = -1.06$  mag and  $+\sigma_3^+ = +1.74$  mag.

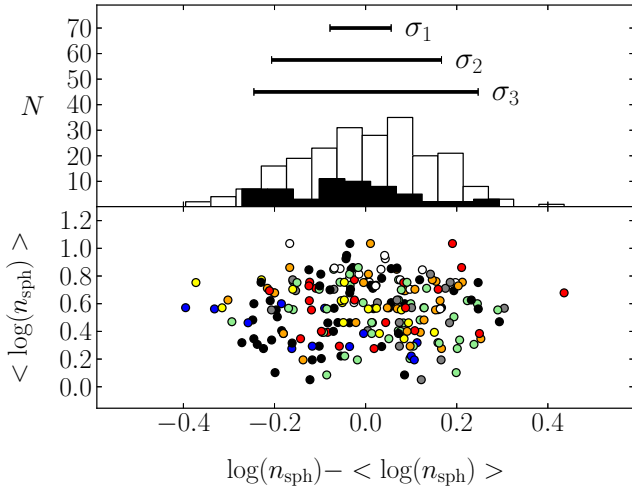


FIG. 9.— The bottom panel shows 58 galaxies for which at least one measurement of the bulge Sérsic index  $n_{\text{sph}}$  is available from the literature, in addition to that measured by us. In ordinate, for each galaxy, we plot the average value  $\langle \log(n_{\text{sph}}) \rangle$  of (the logarithm of) the individual measurements. In abscissa we plot the difference between (the logarithm of) the individual measurements of a galaxy and the average value for that same galaxy. Each data point corresponds to an individual measurement, which comes from one of the following studies. Red points are from Graham & Driver (2007a), blue points are from Laurikainen et al. (2010), green points are from Sani et al. (2011), yellow points are from Vika et al. (2012), gray points are from Beifiori et al. (2012), white points are from Rusli et al. (2013a), orange points are from Läsker et al. (2014a), and black points are measurements obtained from the 1D fits presented in this work (using linearly sampled surface brightness profiles, along the major-axis). In the top panel, the white histogram shows the distribution of  $\log(n_{\text{sph}}) - \langle \log(n_{\text{sph}}) \rangle$  for all measurements, whereas the black histogram refers only to measurements obtained by us. The (asymmetric) error bars  $\sigma_1$ ,  $\sigma_2$  and  $\sigma_3$  enclose 38%, 78% and 92% of the black histogram, respectively.

#### 4.2.6. Uncertainties on $\mu_{0,\text{sph}}$

From the values of  $\mu_{\text{e},\text{sph}}$ , we derived the central surface brightnesses  $\mu_{0,\text{sph}}$  as

$$\mu_{0,\text{sph}} = \mu_{\text{e},\text{sph}} - \frac{2.5b_n}{\ln(10)}. \quad (4)$$

The associated  $1\sigma$  uncertainties for our measurements of  $\mu_{0,\text{sph}}$  are  $-\sigma_1^- = -0.20$  mag and  $+\sigma_1^+ = +0.64$  mag,  $-\sigma_2^- = -0.70$  mag and  $+\sigma_2^+ = +1.24$  mag, and  $-\sigma_3^- = -1.05$  mag and  $+\sigma_3^+ = +1.57$  mag.

## 5. CONCLUSIONS

The widespread presence of embedded components – such as intermediate-scale disks – in massive early-type galaxies makes galaxy decomposition an essential tool to properly investigate the scaling relations between black hole masses and host bulge properties.

The bulge best-fit parameters are model-dependent. Past studies often used different models for the same galaxy, and obtained significantly discrepant results, which led them to draw contrasting conclusions about the black hole-bulge correlations. These inconsistencies motivated our effort to secure and refine the measure of bulge properties in a sample of 75 galaxies with a dynamical estimate of the black hole mass. Using  $3.6 \mu\text{m}$  *Spitzer* satellite imagery, we performed state-of-the-art

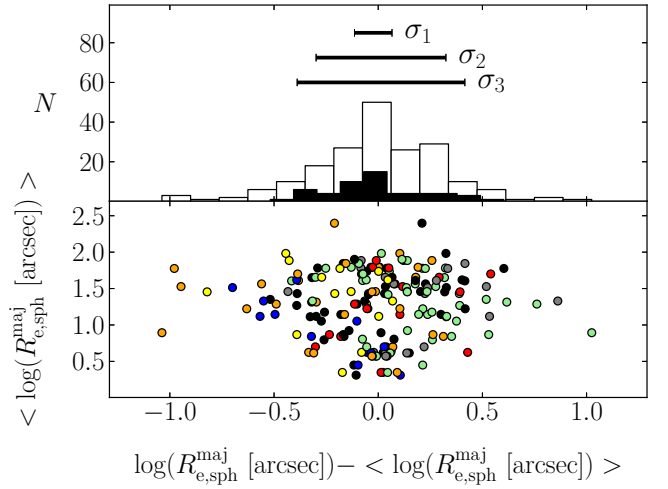


FIG. 10.— The bottom panel shows 52 galaxies for which at least one measurement of the major-axis effective radius  $R_{\text{e}}^{\text{maj}}$  is available from the literature, in addition to that measured by us. In ordinate, for each galaxy, we plot the average value  $\langle \log(R_{\text{e}}^{\text{maj}}) \rangle$  of (the logarithm of) the individual measurements. In abscissa we plot the difference between (the logarithm of) the individual measurements of a galaxy and the average value for that same galaxy. Each data point corresponds to an individual measurement, which comes from one of the following studies. Red points are from Graham & Driver (2007a), blue points are from Laurikainen et al. (2010), green points are from Sani et al. (2011), yellow points are from Vika et al. (2012), gray points are from Beifiori et al. (2012), orange points are from Läsker et al. (2014a), and black points are measurements obtained from the 1D fits presented in this work (using linearly sampled surface brightness profiles, along the major-axis). In the top panel, the white histogram shows the distribution of  $\log(R_{\text{e}}^{\text{maj}}) - \langle \log(R_{\text{e}}^{\text{maj}}) \rangle$  for all measurements, whereas the black histogram refers only to measurements obtained by us. The (asymmetric) error bars  $\sigma_1$ ,  $\sigma_2$  and  $\sigma_3$  enclose 38%, 78% and 92% of the black histogram, respectively.

galaxy decompositions. We compared our best-fit models with those from the past literature, and explained discrepancies when present. Table 4 summarizes the main characteristics of the five past studies that, since 2007, attempted galaxy decomposition to derive black hole-bulge scaling relations, and highlights why our endeavor represents a substantial improvement over the past literature. Our sample of galaxies is the largest ever used. The  $3.6 \mu\text{m}$  band is an excellent tracer for the stellar mass, superior to optical bands or the *K*-band. Läsker et al. (2014a) and this work identified and modeled more galaxy components than any other study, and therefore obtained more accurate decompositions, but we are the first that did it with the assistance of kinematical information.

Our principal conclusions are summarized in the following points.

- One-dimensional and two-dimensional techniques of galaxy decomposition return the same results when applied to the same galaxy. However, in our practical experience, two-dimensional decompositions **HOW DO YOU WRITE THIS IN ENGLISH??** fail twice as much as one-dimensional ones, either because the fit does not converge or because the result is unphysical. A strong limitation of two-dimensional codes is their

TABLE 4

Summary of previous investigations of black hole mass scaling relations. GD07 = GRAHAM & DRIVER (2007A), S+11 = SANI ET AL. (2011), V+12 VIKÄ ET AL. (2012), B+12 = BEIFIORI ET AL. (2012), L+14 = LÄSKER ET AL. (2014A).

	GD07	S+11	V+12	B+12	L+14	This work
Galaxies with successful fit	27	57	25	19	35	66
Wavelength	<i>R</i> -band	3.6 $\mu$ m	<i>K</i> -band	<i>i</i> -band	<i>K</i> -band	3.6 $\mu$ m
Decomposition	1D	2D	2D	2D	2D	1D & 2D
Nuclear components	masked	modeled	modeled	not treated	modeled	modeled/masked
Partially depleted cores	masked	masked	masked	not treated	masked	masked
Bars	excluded	modeled	modeled	excluded	modeled	modeled
Other components	no	no	no	no	yes	yes
Kinematics	no	no	no	no	no	yes

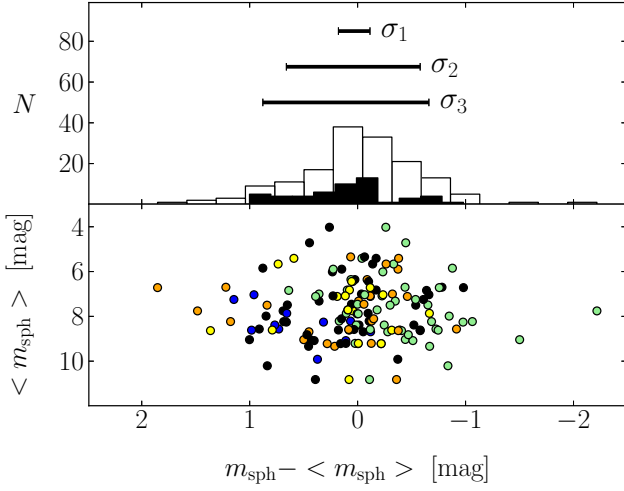


FIG. 11.— The bottom panel shows 51 galaxies for which at least one measurement of the bulge apparent magnitude  $m_{\text{sph}}$  — either in *K*-band or 3.6  $\mu$ m — is available from the literature, in addition to that measured by us. 3.6  $\mu$ m magnitudes were converted to *K*-band magnitudes. In ordinate, for each galaxy, we plot the average value  $\langle m_{\text{sph}} \rangle$  of the individual measurements. In abscissa we plot the difference between the individual measurements of a galaxy and the average value for that same galaxy. Each data point corresponds to an individual measurement, which comes from one of the following studies. Blue points are from Laurikainen et al. (2010), green points are from Sani et al. (2011), yellow points are from Vika et al. (2012), orange points are from Läsker et al. (2014a), and black points are measurements obtained from the 1D fits presented in this work (using linearly sampled surface brightness profiles, along the equivalent-axis). In the top panel, the white histogram shows the distribution of  $m_{\text{sph}} - \langle m_{\text{sph}} \rangle$  for all measurements, whereas the black histogram refers only to measurements obtained by us. The (asymmetric) error bars  $\sigma_1$ ,  $\sigma_2$  and  $\sigma_3$  enclose 38%, 78% and 92% of the black histogram, respectively.

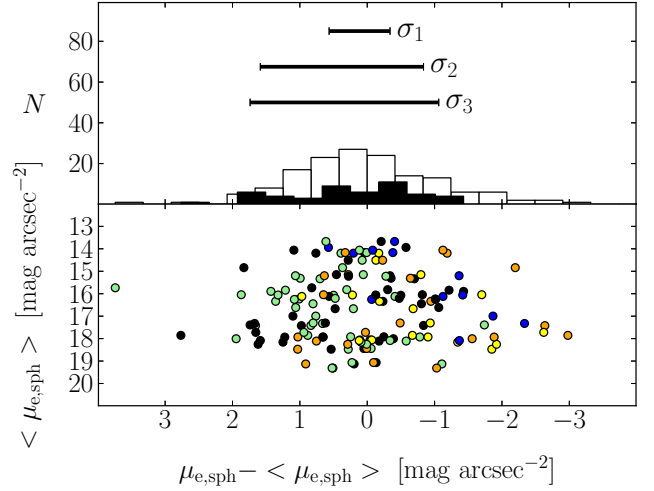


FIG. 12.— The bottom panel shows 49 galaxies for which at least one measurement of the bulge effective surface brightness  $\mu_{\text{e,sph}}$  — either in *K*-band or 3.6  $\mu$ m — is available from the literature, in addition to that measured by us. *K*-band magnitudes were converted to 3.6  $\mu$ m magnitudes. In ordinate, for each galaxy, we plot the average value  $\langle \mu_{\text{e,sph}} \rangle$  of the individual measurements. In abscissa we plot the difference between the individual measurements of a galaxy and the average value for that same galaxy. Each data point corresponds to an individual measurement, which comes from one of the following studies. Blue points are from Laurikainen et al. (2010), green points are from Sani et al. (2011), yellow points are from Vika et al. (2012), orange points are from Läsker et al. (2014a), and black points are measurements obtained from the 1D fits presented in this work (using linearly sampled surface brightness profiles, along the major-axis). In the top panel, the white histogram shows the distribution of  $\mu_{\text{e,sph}} - \langle \mu_{\text{e,sph}} \rangle$  for all measurements, whereas the black histogram refers only to measurements obtained by us. The (asymmetric) error bars  $\sigma_1$ ,  $\sigma_2$  and  $\sigma_3$  enclose 38%, 78% and 92% of the black histogram, respectively.

inability to accommodate the radial gradients of ellipticity and position angle often observed in galaxy bulges.

- We found the interpretation of one-dimensional residuals easier than that of two-dimensional residual images. A correct interpretation of the residuals is fundamental to determine the optimal model for a galaxy.
- A one-dimensional isophotal analysis was extremely helpful and sometimes even necessary to accurately identify galaxy components.
- Given the level of detail to which each galaxy decomposition was performed, we believe that our

analysis cannot be reproduced by any current automatic routine.

- The uncertainties associated with the bulge best-fit parameters are dominated by systematic errors (e.g. incorrect sky subtraction, inaccurate masking of contaminating sources, erroneous choice of model components), and only marginally affected by random errors. For this reason, we developed a method to estimate the uncertainties on the best-fit parameters that takes into account systematic errors.

We will use the results from our one-dimensional galaxy decompositions to obtain improved black hole mass scaling relations. We will also derive and explore

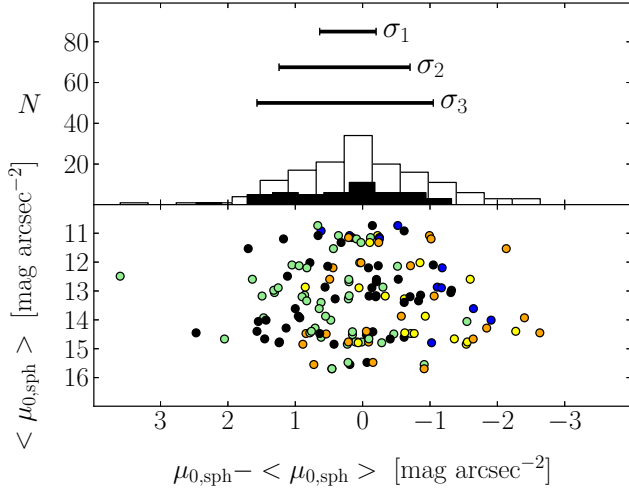


FIG. 13.— The bottom panel shows 49 galaxies for which at least one measurement of the bulge central surface brightness  $\mu_{0,\text{sph}}$  — either in  $K$ -band or  $3.6\ \mu\text{m}$  — is available from the literature, in addition to that measured by us.  $K$ -band magnitudes were converted to  $3.6\ \mu\text{m}$  magnitudes. In ordinate, for each galaxy, we plot the average value  $\langle\mu_{0,\text{sph}}\rangle$  of the individual measurements. In abscissa we plot the difference between the individual measurements of a galaxy and the average value for that same galaxy. Each data point corresponds to an individual measurement, which comes from one of the following studies. Blue points are from Laurikainen et al. (2010), green points are from Sani et al. (2011), yellow points are from Vika et al. (2012), orange points are from Läsker et al. (2014a), and black points are measurements obtained from the 1D fits presented in this work (using linearly sampled surface brightness profiles, along the major-axis). In the top panel, the white histogram shows the distribution of  $\mu_{0,\text{sph}} - \langle\mu_{0,\text{sph}}\rangle$  for all measurements, whereas the black histogram refers only to measurements obtained by us. The (asymmetric) error bars  $\sigma_1$ ,  $\sigma_2$  and  $\sigma_3$  enclose 38%, 78% and 92% of the black histogram, respectively.

## APPENDIX

### 1D ANALYTICAL FUNCTIONS

Below we give the mathematical expressions of all the analytical functions used in this work to model the observed surface brightness profiles ( $\mu$ ) of galaxies. We indicate with  $R$  the projected galactic radius, corresponding to the distance of the isophotes from the galaxy center (along the major- or equivalent-axis).

The *Sérsic profile* (Sérsic 1963; Sérsic 1968) is a three-parameter function with the following form:

$$\mu_{\text{Sérsic}}(\mu_e, R_e, n; R) = \mu_e + \frac{2.5\ b_n}{\ln(10)} \left[ \left( \frac{R}{R_e} \right)^{1/n} - 1 \right], \quad (\text{A1})$$

(Caon et al. 1993; Andredakis et al. 1995; Graham & Driver 2005) where  $\mu_e$  is the surface brightness at the effective radius  $R_e$  that encloses half of the total light from the model, the Sérsic index  $n$  is the parameter that measures the curvature of the radial light profile, and  $b_n$  is a scalar value defined in terms of the Sérsic index  $n$ . The value of  $b_n$  is found by solving numerically the following expression:

$$\Gamma(2n) = 2\gamma(2n, b_n), \quad (\text{A2})$$

where  $\Gamma$  is the complete gamma function (Ciotti 1991) and  $\gamma$  is the incomplete gamma function defined by

$$\gamma(2n, x) = \int_0^x e^{-t} t^{2n-1} dt. \quad (\text{A3})$$

The *exponential profile* is a special case ( $n = 1$ ) of the Sérsic profile. It is therefore a two-parameter function, with the following form:

$$\mu_{\text{exponential}}(\mu_0, h; R) = \mu_0 + \frac{2.5}{\ln(10)} \left( \frac{R}{h} \right), \quad (\text{A4})$$

some unpublished correlations. These results will be presented in a series of forthcoming papers.

GS warmly thanks Chieng Peng, Peter Erwin, Luca Cortese, Elisabete Lima Da Cunha and Gonzalo Diaz for useful discussion.

This research was supported by Australian Research Council funding through grants DP110103509 and FT110100263. This work is based on observations made with the IRAC instrument (Fazio et al. 2004) on-board the Spitzer Space Telescope, which is operated by the Jet Propulsion Laboratory, California Institute of Technology under a contract with NASA. This research has made use of the GOLDMine database (Gavazzi et al. 2003) and the NASA/IPAC Extragalactic Database (NED) which is operated by the Jet Propulsion Laboratory, California Institute of Technology, under contract with the National Aeronautics and Space Administration.

where  $\mu_0$  is the central surface brightness and  $h$  is the scale length.

The *Gaussian profile* is a two-parameter function with the following form:

$$\mu_{\text{Gaussian}}(\mu_0, FWHM; R) = \mu_0 + \frac{2.5}{\ln(10)} \left[ \frac{R^2}{2(FWHM/2.355)^2} \right], \quad (\text{A5})$$

where  $\mu_0$  is the central surface brightness and  $FWHM$  is the full width at half maximum of the Gaussian profile.

The *Moffat profile* (Moffat 1969) is a three-parameter function with the following form:

$$\mu_{\text{Moffat}}(\mu_0, \alpha, \beta; R) = \mu_0 - 2.5 \log \left[ 1 + \left( \frac{R}{\alpha} \right)^2 \right]^{-\beta}, \quad (\text{A6})$$

where  $\mu_0$  is the central surface brightness,  $\alpha$  is related to the  $FWHM$  through

$$FWHM = 2\alpha \sqrt{2^{1/\beta} - 1} \quad (\text{A7})$$

and  $\beta$  regulates the shape of the profile at large radii.

The *Ferrer profile* is a four-parameter function with the following form:

$$\mu_{\text{Ferrer}}(\mu_0, R_{\text{out}}, \alpha, \beta; R) = \begin{cases} \mu_0 - 2.5 \log \left[ 1 - \left( \frac{R}{R_{\text{out}}} \right)^{2-\beta} \right]^\alpha & \text{for } R < R_{\text{out}} \\ +\infty & \text{for } R \geq R_{\text{out}} \end{cases}, \quad (\text{A8})$$

where  $\mu_0$  is the central surface brightness,  $\alpha$  controls the sharpness of the truncation,  $\beta$  is related to the central slope, and  $R_{\text{out}}$  is the limit within which the function is defined.

The *symmetric Gaussian ring* is a three-parameter function with the following form:

$$\mu_{\text{Gaussian}}(\mu_0, R_0, FWHM; R) = \mu_0 + \frac{2.5}{\ln(10)} \left[ \frac{(R - R_0)^2}{2(FWHM/2.355)^2} \right], \quad (\text{A9})$$

where  $\mu_0$  is the central surface brightness,  $R_0$  is the radius at which the Gaussian profile is centered, and  $FWHM$  is the full width at half maximum of the Gaussian profile.

## REFERENCES

- Andredakis, Y. C., Peletier, R. F., & Balcells, M. 1995, *MNRAS*, 275, 874
- Arnold, J. A., Romanowsky, A. J., Brodie, J. P., et al. 2014, *ApJ*, 791, 80
- Beifiori, A., Courteau, S., Corsini, E. M., & Zhu, Y. 2012, *MNRAS*, 419, 2497
- Bender, R. 1990, *A&A*, 229, 441
- Caon, N., Capaccioli, M., & D’Onofrio, M. 1993, *MNRAS*, 265, 1013
- Capaccioli, M. 1987, in *IAU Symposium*, Vol. 127, *Structure and Dynamics of Elliptical Galaxies*, ed. P. T. de Zeeuw, 47–60
- Cappellari, M., Emsellem, E., Krajnović, D., et al. 2011, *MNRAS*, 413, 813
- Carter, D. 1987, *ApJ*, 312, 514
- Ciotti, L. 1991, *A&A*, 249, 99
- Comastri, A., Gilli, R., Marconi, A., Risaliti, G., & Salvati, M. 2015, *ArXiv e-prints*, arXiv:1501.03620
- de Vaucouleurs, G., de Vaucouleurs, A., Corwin, Jr., H. G., et al. 1991, *Third Reference Catalogue of Bright Galaxies. Volume I: Explanations and references. Volume II: Data for galaxies between 0<sup>h</sup> and 12<sup>h</sup>. Volume III: Data for galaxies between 12<sup>h</sup> and 24<sup>h</sup>.*
- D’Onofrio, M., Zaggia, S. R., Longo, G., Caon, N., & Capaccioli, M. 1995, *A&A*, 296, 319
- Dressler, A. 1989, in *IAU Symposium*, Vol. 134, *Active Galactic Nuclei*, ed. D. E. Osterbrock & J. S. Miller, 217
- Dullo, B. T., & Graham, A. W. 2013, *ArXiv e-prints*, arXiv:1310.5867
- Emsellem, , & E. et al. 2011, *MNRAS*, 414, 888
- Erwin, P. 2015, *ApJ*, 799, 226
- Fazio, G. G., Hora, J. L., Allen, L. E., et al. 2004, *ApJS*, 154, 10
- Ferrarese, L., & Merritt, D. 2000, *ApJ*, 539, L9
- Ferrarese, L., Côté, P., Jordán, A., et al. 2006, *ApJS*, 164, 334
- Forbes, D. A., Brodie, J. P., & Huchra, J. 1997, *AJ*, 113, 887
- Gavazzi, G., Boselli, A., Donati, A., Franzetti, P., & Scodreggio, M. 2003, *A&A*, 400, 451
- Gebhardt, K., Bender, R., Bower, G., et al. 2000, *ApJ*, 539, L13
- Graham, A. W. 2012, *ApJ*, 746, 113
- . 2015, *ArXiv e-prints*, arXiv:1501.02937
- Graham, A. W., Colless, M. M., Busarello, G., Zaggia, S., & Longo, G. 1998, *A&AS*, 133, 325
- Graham, A. W., & Driver, S. P. 2005, *PASA*, 22, 118
- . 2007a, *ApJ*, 655, 77
- . 2007b, *MNRAS*, 380, L15
- Graham, A. W., Driver, S. P., Allen, P. D., & Liske, J. 2007, *MNRAS*, 378, 198
- Graham, A. W., Erwin, P., Caon, N., & Trujillo, I. 2001, *ApJ*, 563, L11
- Graham, A. W., Erwin, P., Trujillo, I., & Asensio Ramos, A. 2003, *AJ*, 125, 2951
- Graham, A. W., & Guzmán, R. 2003, *AJ*, 125, 2936
- Graham, A. W., & Scott, N. 2013, *ApJ*, 764, 151
- . 2015, *ApJ*, 798, 54
- Greenhill, L. J., Booth, R. S., Ellingsen, S. P., et al. 2003, *ApJ*, 590, 162
- Grillmair, C. J., Faber, S. M., Lauer, T. R., et al. 1994, *AJ*, 108, 102
- Häring, N., & Rix, H.-W. 2004, *ApJ*, 604, L89
- Haynes, M. P., Giovanelli, R., Salzer, J. J., et al. 1999, *AJ*, 117, 1668

- Jardel, J. R., Gebhardt, K., Shen, J., et al. 2011, *ApJ*, 739, 21
- Jedrzejewski, R. I. 1987, *MNRAS*, 226, 747
- King, I. R., & Minkowski, R. 1966, *ApJ*, 143, 1002
- Kormendy, J., & Richstone, D. 1995, *ARA&A*, 33, 581
- Krajinović, D., Emsellem, E., Cappellari, M., et al. 2011, *MNRAS*, 414, 2923
- Krajinović, D., Alatalo, K., Blitz, L., et al. 2013, *MNRAS*, 432, 1768
- Laor, A., Fiore, F., Elvis, M., Wilkes, B. J., & McDowell, J. C. 1997, *ApJ*, 477, 93
- Läsker, R., Ferrarese, L., & van de Ven, G. 2014a, *ApJ*, 780, 69
- Läsker, R., Ferrarese, L., van de Ven, G., & Shankar, F. 2014b, *ApJ*, 780, 70
- Laurikainen, E., Salo, H., Buta, R., Knapen, J. H., & Comerón, S. 2010, *MNRAS*, 405, 1089
- Magorrian, J., Tremaine, S., Richstone, D., et al. 1998, *AJ*, 115, 2285
- Makovoz, D., & Marleau, F. R. 2005, *PASP*, 117, 1113
- Marconi, A., & Hunt, L. K. 2003, *ApJ*, 589, L21
- Moffat, A. F. J. 1969, *A&A*, 3, 455
- Nieto, J.-L., Bender, R., Arnaud, J., & Surma, P. 1991, *A&A*, 244, L25
- Pastrav, B. A., Popescu, C. C., Tuffs, R. J., & Sansom, A. E. 2013a, *A&A*, 553, A80
- . 2013b, *A&A*, 557, A137
- Peng, C. Y., Ho, L. C., Impey, C. D., & Rix, H.-W. 2010, *AJ*, 139, 2097
- Quillen, A. C., Bower, G. A., & Stritzinger, M. 2000, *ApJS*, 128, 85
- Richings, A. J., Uttley, P., & Körding, E. 2011, *MNRAS*, 415, 2158
- Richstone, D., Ajhar, E. A., Bender, R., et al. 1998, *Nature*, 395, A14
- Rix, H.-W., & White, S. D. M. 1990, *ApJ*, 362, 52
- . 1992, *MNRAS*, 254, 389
- Rusli, S. P., Erwin, P., Saglia, R. P., et al. 2013a, *AJ*, 146, 160
- Rusli, S. P., Thomas, J., Saglia, R. P., et al. 2013b, *AJ*, 146, 45
- Salucci, P., Szuszkiewicz, E., Monaco, P., & Danese, L. 1999, *MNRAS*, 307, 637
- Sani, E., Marconi, A., Hunt, L. K., & Risaliti, G. 2011, *MNRAS*, 413, 1479
- Savorgnan, G. A. D., & Graham, A. W. 2014, *ArXiv e-prints*, arXiv:1410.7405
- Schaye, J., Crain, R. A., Bower, R. G., et al. 2015, *MNRAS*, 446, 521
- Scorza, C., & Bender, R. 1990, *A&A*, 235, 49
- . 1995, *A&A*, 293, 20
- Scott, N., Davies, R. L., Houghton, R. C. W., et al. 2014, *MNRAS*, 441, 274
- Sérsic, J. L. 1963, *Boletín de la Asociación Argentina de Astronomía La Plata Argentina*, 6, 41
- Sersic, J. L. 1968, *Atlas de galaxias australes*
- Sheth, K., Regan, M., Hinz, J. L., et al. 2010, *PASP*, 122, 1397
- Tran, H. D., Tsvetanov, Z., Ford, H. C., et al. 2001, *AJ*, 121, 2928
- Trujillo, I., Erwin, P., Asensio Ramos, A., & Graham, A. W. 2004, *AJ*, 127, 1917
- Trujillo, I., Graham, A. W., & Caon, N. 2001, *MNRAS*, 326, 869
- Véron-Cetty, M.-P., & Véron, P. 2006, *A&A*, 455, 773
- Vika, M., Driver, S. P., Cameron, E., Kelvin, L., & Robotham, A. 2012, *MNRAS*, 419, 2264
- Worthey, G. 1994, *ApJS*, 95, 107
- Yee, H. K. C. 1992, in *Astronomical Society of the Pacific Conference Series*, Vol. 31, *Relationships Between Active Galactic Nuclei and Starburst Galaxies*, ed. A. V. Filippenko, 417